POLITECNICO DI MILANO

School of Industrial and Information Engineering

Master's degree in Materials Engineering and Nanotechnology
Chemistry, Materials and Chemical Engineering Department "Giulio Natta"

Highly fluorinated anions as potential water-soluble probes for ^{19}F-MRI

Supervisor: Prof. Pierangelo METRANGOLO

Co-supervisor: Dott.ssa Valentina DICHIARANTE

Master Thesis of:

Mattia Russo

CARRER ID 899774

Academic Year 2020-2021

Ringraziamenti

Giunto al termine di questo percorso intenso che mi ha fatto crescere e insegnato tanto, desidero ringraziare tutte le persone che mi hanno accompagnato durante questo anno particolare, aiutandomi a realizzare questo progetto. Innanzitutto voglio ringraziare il Professor Pierangelo Metrangolo per l'opportunità che mi ha concesso e per la fiducia nell'affidarmi questo progetto di tesi. Un grazie enorme alla Dott.ssa Valentina Dichiarante per tutto il supporto e il tempo dedicatomi. Nonostante sommersa da impegni istituzionali, lezioni e progetti di ricerca, non mi ha mai fatto mancare il suo aiuto e la sua disponibilità; mi ha insegnato come gestire un progetto di laboratorio e diventare autonomo. Ringrazio tutto il gruppo di ricerca SupraBioNanoLab: Marta, Lorenzo, Andrea, Cristina, Alessandro, Beatrice ed Eleonora per avermi fatto sentire accolto fin dal primo giorno all' interno di un bellissimo gruppo di ricerca, per essere sempre stati pronti ad aiutarmi e per avermi sostenuto anche quando non tutto andava per il verso giusto. Vorrei fare un ringraziamento speciale anche a te Fede per averi sopportato, sostenuto e soprattutto ascoltato in questi lunghi anni di università. Infine vorrei tanto ringraziare la mia famiglia: papà, mamma e Silvia; grazie per avermi permesso di poter realizzare questo mio grande sogno e per tutto l'amore che mi avete dato.

Abstract

Magnetic Resonance Imaging (MRI) is one of the most promising non-invasive diagnostic techniques for monitoring various diseases and for developing targeted therapies without the use of radioactive nuclides or ionizing radiations. Among all the available magnetically active isotopes, fluorine-19 (^{19}F) seems particularly promising due to the absence of endogenous signals in the body, allowing the direct detection of externally administered fluorinated tracers and labelled cells with unambiguous identification and quantification. Up to now, the most commonly used ^{19}F-MRI probes have been perfluoro- and polyfluorocarbons, which unfortunately are insoluble in water and need to be dispersed in aqueous media by means of surfactants before use.

This thesis aimed to perform a preliminary study on the possibility to use the highly fluorinated anion $[Al(OC(CF_3)_3)_4]^-$, whose structure with 36 magnetically equivalent ^{19}F atoms resembles that of the previously reported ^{19}F-MRI superfluorinated probe PERFECTA, as a potential water-soluble ^{19}F MRI tracer, avoiding the use of emulsifiers or other dispersing agents. After an initial assessment of its maximum solubility in water, several solubilisation methods were tested in order to maximize the amount of dissolved fluorinated anion, as well as to remove bigger insoluble aggregates by filtration and centrifugation. The resulting solutions were characterized by Dynamic Light Scattering (DLS) and ^{19}F Nuclear Magnetic Resonance (^{19}F-NMR), always showing a sharp singlet peak with good stability over time. Similar dissolution and stability tests were performed in media resembling physiological fluids, such as phosphate buffer saline (PBS) solution, proving that a clear and sharp ^{19}F-NMR signal was still visible. Despite these good premises, a preliminary ^{19}F-MR phantom imaging trial, performed on the most concentrated sample, showed that a further optimization of the dispersion protocol in water would be required in order to improve the MRI signal intensity. A possible future strategy could envisage the encapsulation of the anion into some biocompatible and water-soluble carrier, to avoid also undesired and destabilizing interactions with proteins or other biomolecules that are normally present in physiological liquids.

Sommario

La Magnetic Resonance Imaging (MRI) è una delle più promettenti tecniche di diagnostica non invasiva per il monitoraggio di varie malattie e per lo sviluppo di terapie mirate senza l'utilizzo di nuclidi radioattivi o radiazioni ionizzanti. Tra tutti gli isotopi magneticamente attivi disponibili il fluoro-19 (^{19}F) sembra essere particolarmente promettente grazie all'assenza di segnali endogeni nel corpo, permettendo il rilevamento diretto dei traccianti fluorurati somministrati esternamente e di cellule marcate con identificazione e quantificazione univoche. Al momento i più comuni traccianti utilizzati per ^{19}F-MRI sono i perfluoro – and polifluorocarburi, che purtroppo sono insolubili in acqua e quindi necessitano di essere dispersi in mezzi acquosi mediante tensioattivi prima dell'uso.

Questa tesi mira a svolgere uno studio preliminare sul possibile uso dell'anione altamente fluorurato $[Al(OC(CF_3)_3)_4]^-$, la cui struttura con 36 ^{19}F atomi magneticamente equivalenti ricorda quella del precedentemente citato ^{19}F tracciante superfluorinato PERFECTA, come possibile tracciante per ^{19}F-MRI, evitando l'utilizzo di emulsionanti o altri agenti disperdenti. Dopo una prima valutazione della sua massima solubilità in acqua, sono stati testati diversi metodi di solubilizzazione in modo da massimizzare la quantità di anione fluorurato disciolto, come, ad esempio, la rimozione degli aggregati insolubili più grandi mediante filtrazione e centrifugazione. Le soluzioni ottenute sono state caratterizzate mediante Dynamic Light Scattering (DLS) e ^{19}F Nuclear Magnetic Resonance (^{19}F-NMR) e mostrano sempre un singolo e definito picco, con una buona stabilità nel tempo. Test di dissoluzione e stabilità sono stati eseguiti anche in mezzi simili a fluidi fisiologici, come la soluzione salina di tampone fosfato (PBS), dimostrando la presenza di un segnale ^{19}F-NMR ancora definito e nitido. Nonostante queste buone premesse, una prova preliminare di imaging ^{19}F-MR di un phantom, eseguita sul campione più concentrato, ha mostrato che è necessario una ulteriore ottimizzazione del protocollo di dispersione in acqua per migliorare l'intensità del segnale MRI. Una possibile strategia futura potrebbe prevedere l'incapsulamento dell'anione in qualche vettore biocompatibile e

solubile in acqua per evitare indesiderate e destabilizzanti interazioni con proteine o altre biomolecole normalmente presenti in liquidi fisiologici.

INDEX

Chapter 1: Introduction

1.1 Molecular Imaging

Molecular imaging allows to characterize and quantify biological processes at the cellular and subcellular level in intact living subjects. It usually exploits specific molecular probes, as well as intrinsic tissue characteristics as the source of image contrast, providing earlier detection and characterization of diseases, and evaluation of the possible treatments. Although still in its infancy, molecular imaging is showing enormous promise in the areas of diagnostics, therapy monitoring, drug discovery and development, and in understanding nanoscale reactions, such as protein-protein interactions and enzymatic conversion [1]. One of the main goal of molecular imaging is to overcome existing limitations of the most used in vitro techniques, such as electric cell-substrate impedance sensing, dye exclusion assays, colony formation assay. These limitations are: *i*) the inability to provide analyses of entire intact organisms over time, making it difficult to appreciate the "full picture" of disease states and/or biochemical process; *ii*) the required removal of cell, organ, or tissue samples from their natural environment and/or the need for preparing samples altering physiological conditions; *iii*) the fact that samples (e.g., brain tissue slices) can often only be analysed by one or two in vitro techniques, due to the destruction or irreversible alteration of the sample; and *iv*) the necessary euthanasia of animals, making impossible further studies on the same animal, and creating issues with regards to both costs and ethics [2]. For these reasons, there has been a great need for methods that allow to visualize and to study biochemical processes in intact living subjects, noninvasively and over time. Compared with traditional in vitro methods, molecular imaging approaches have a number of advantages. It is possible, via different molecular imaging techniques, the non-invasive study of cells in their natural microenvironment, without perturbing the system under investigation, and to trace the movement of cells understanding dynamic biological processes (e.g., tracking the location of therapeutic cytolytic T cells in a patient with glioma). Most

available molecular imaging techniques may be conducted with adequate temporal and spatial resolution for studying intricate biological and physiological processes in living subjects. Moreover, rapid information concerning pharmaceuticals can be obtained, thereby reducing the amount of time it takes to evaluate the efficacy, metabolism, and safety profile of a potential therapeutic [3]. Currently, there are several in vivo imaging techniques that allow the detection of molecular targets, and provide different biological information (anatomical and/or metabolic). Magnetic resonance spectroscopy (MRS), single-photon-emission computed tomography (SPECT), positron emission tomography (PET) and magnetic resonance imaging (MRI) are some of the most used imaging techniques in human diagnostic [4]. MRS is an analytical tool that detects radio frequency electromagnetic signals that are produced by the atomic nuclei within molecules. It can be used to obtain in situ concentration measures for certain chemicals in complex samples, such as the living brain [5]. PET scan uses a radioactive tracer, which can be injected, swallowed or inhaled. The tracer collects in areas of the body that have higher levels of chemical activity, which often correspond to areas of disease [6]. SPECT is based on the detection of gamma rays emitted by the radionuclides embedded in biologically specific compounds after the injection of the compounds into humans or experimental animals. The most common imaging radionuclides emit gamma rays, which are uncorrelated, and these gamma rays are detected individually or singularly for imaging [7]. Differently from the techniques described above, MRI is one of the most promising non-invasive diagnostic techniques for the monitoring of various diseases and, the development of targeted therapies without the use of radioactive nuclides or ionizing radiations [4]. MRI will be the final application of this thesis' work, thus it requires a discussion to explain the fundamentals of this diagnostic techniques.

1.2 Magnetic Resonance Imaging (MRI)

The basics of imaging by nuclear magnetic resonance (NMR), explained by Lauterbur in the 1970s, depend on the ability of hydrogen atoms (^1H) to align in the direction of an external magnetic field [8], **Fig. 1.**

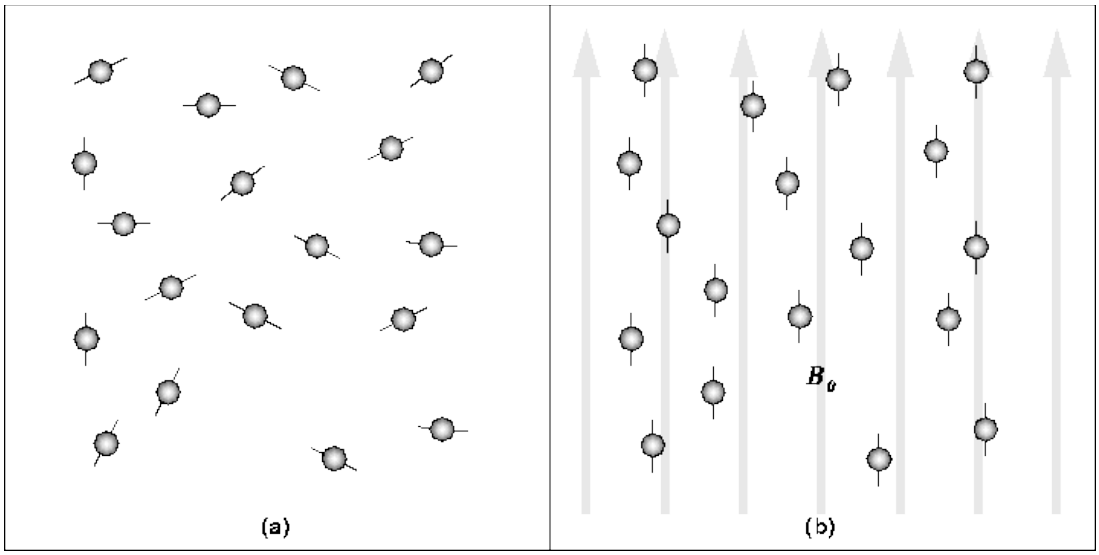

Figure 1: In the absence of a strong magnetic field, hydrogen nuclei are randomly aligned as in (a). When a strong magnetic field, B_0, is applied, hydrogen nuclei precess about the direction of the field as in (b) [9].

Hydrogen nuclei are single protons with a proper magnetic moment, which is normally randomly oriented. When an external static magnetic field (B_0) is applied, protons' magnetic moments can align to the external field either in parallel or anti-parallel direction. These directions of alignment correspond to two energy states, respectively at lower and higher energy; the nucleus does not orientate completely because it has an angular momentum due to its rotation, so it will rotate, or precess, around the B_0 axis like a gyroscope. This behavior is termed Larmor precession. The Larmor frequency (ω_0), or the precession frequency, is proportional to the applied magnetic field strength as defined by **equation 1**:

$$\omega_0 = \Upsilon B_0 \qquad \textbf{Eq.1}$$

where ϒ is the gyromagnetic ratio and B_0 is the strength of the applied magnetic field. The gyromagnetic ratio is a nuclei specific constant. Protons processing parallel to B_0 start to cancel each other out in all the directions except one: the direction of the axis along B_0. By summing up all the contributions in this direction a sum magnetization is obtained, called longitudinal magnetization (M). Next, a radio-frequency (RF) pulse B_{rf}, is applied perpendicular to B_0. This pulse, with a frequency equal to the Larmor frequency, causes M to tilt away from B_0 as in **Fig. 2**. Once the RF signal is removed, the nuclei realign themselves until their net magnetic moment, M, is again parallel with B_0. This return to equilibrium is referred to as relaxation [9].

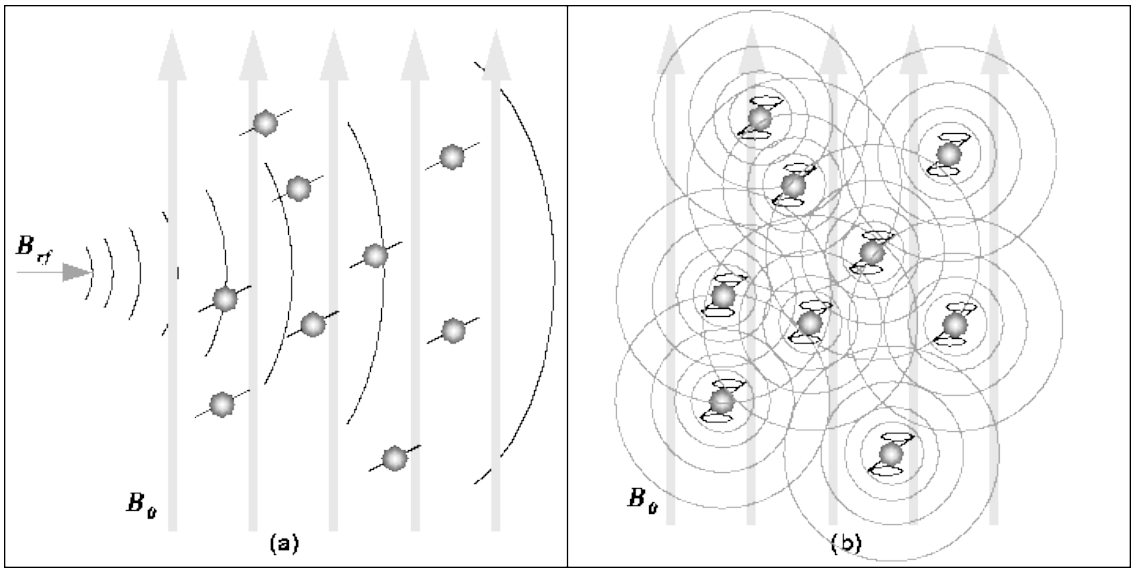

Figure 2: (a) The RF pulse B_{rf}, causes the net magnetic moment of the nuclei M, to tilt away from B_0. (b) When the RF pulse stops, the nuclei return to equilibrium so that M is again parallel to B_0. During realignment, the nuclei lose energy and and this generates a measurable RF signal [9].

There are two types of relaxation processes, longitudinal and transverse relaxations, and these are described by the time constants T_1 and T_2, respectively. T_1 is also known as “spin-lattice relaxation time”, whereby the “lattice” is the environment surrounding the nucleus. As longitudinal relaxation occurs, energy is dissipated into the lattice. T_1 is the length of time taken for the

system to return 63% toward thermal equilibrium following an RF pulse as an exponential function of time. The rate of this relaxation process is different for different tissues and is the fundamental source of contrast in T_1-weighted images.T_1 can be manipulated by varying the times between RF pulses. Whereas T_2 (or spin-spin relaxation time) refers to the time taken for transversal magnetization to drop to 37% of its initial value. Images based on this contrast mechanism are called T_2-weighted [10]. The energy emitted by the nuclei during relaxation induces a voltage that can be detected by a suitably tuned coil of wire, amplified and displayed as the "free-induction decay" (FID). ^{1}H-MRI use the principle described above to provide physiological and anatomical information with high spatial resolution and excellent tissue contrast [11]. In general, according to the composition of the tissue and its water content, one method is preferred than the other [9]. As a matter of fact, T_1-weighted images are good for demonstrating anatomy, as tissues with high fat content appear bright and areas filled with water appears dark. In T_2-weighted images the situation is the opposite and this is the reason why they are good for demonstrating pathology, since most lesions are associated with an increase in water content [12], **Fig. 3.**

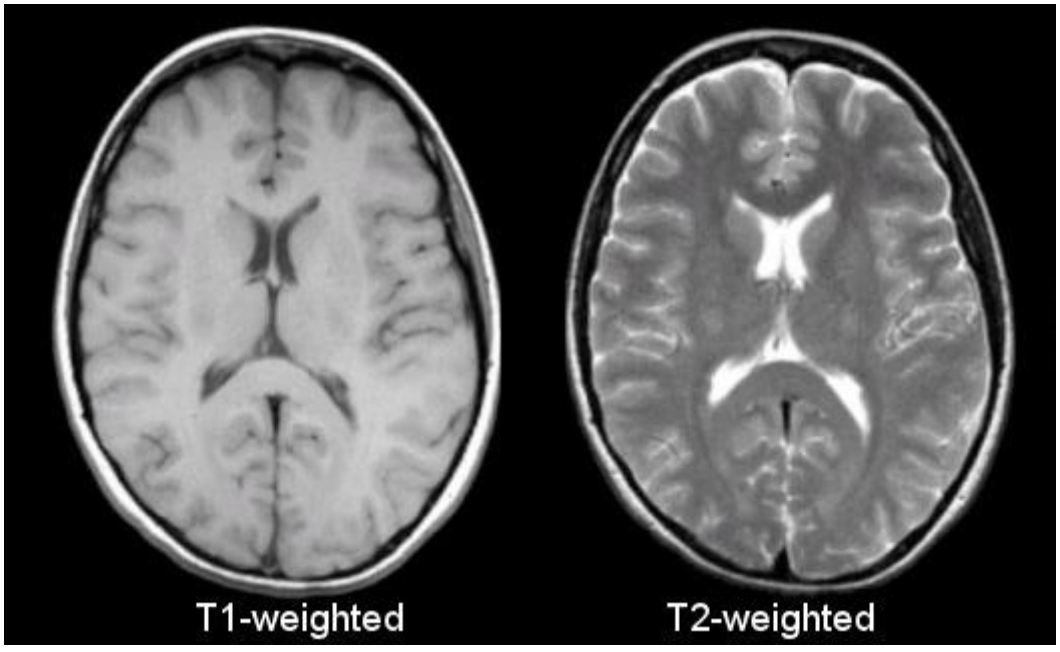

Figure 3. Comparison T1- weighted vs T2- weighted MRI. Adapted from [13].

If, on one side, anatomical resolution is a strength of the MRI technique, its relative insensitivity is a weakness, which requires the use of tailored contrast agents (CAs). The CAs for ^{1}H-MRI are classified as T_1 or T_2 agents: T_1 agents result in hyperintensity, whereas T_2 agents in hypointensity. CAs are not detected directly, but instead they can affect ^{1}H signals of surrounding water, and thus highlight anatomical and pathological features in the imaged tissues by enhancing image contrast [14]. As reported above, each compound (or tissue) has a characteristic T_1 that reflects the time required for signal recovery after an excitation pulse. Thus a shorter T_1, as caused by a T_1 paramagnetic contrast agent, results in faster signal recovery and therefore a brighter (hyperintense) region in the image. Gadolinium (Gd^{3+}) complexes are the most commonly used T_1 agents. The spin–spin relaxation time governs the decay of the signal in the transverse plane. Acceleration of this signal loss by T_2 agents results in a localized dark (hypointense) spot due to the large magnetic field inhomogeneities they create. Superparamagnetic iron oxide (SPIO) is one of the most commonly used T_2 contrast agents for MRI [15]. Despite improvements in the MRI performance of the currently used CAs, they still present some disadvantages: their use generally requires long acquisition times because it is necessary to acquire images before and after their administration; their localization, based on contrast modulation, is often complicated by the high background signal from water, as well as by the intrinsic sources of contrast in tissues, such as blood clots and endogenous iron. Furthermore, the low sensitivity of standard ^{1}H-MRI techniques requires relatively high concentrations of such contrast agents, possibly resulting in toxicity issues [16]. For all these reasons, there is an increasing interest in the development of a ‘second color’ or ‘hot-spot’ imaging – heteronuclear MRI using ^{13}C, ^{23}Na, ^{31}P or ^{19}F, in addition to ^{1}H. The use of these nuclei enables direct detection rather than the indirect detection necessary for contrast agents, thus avoiding the need for pre-scans and removing localization ambiguity. Most of these isotopes are naturally present in biological tissues, and can thus influence the background signal. Among theme, ^{19}F has several properties that make it suitable as an MRI tracer: (*i*) a high relative sensitivity, that is 83% of ^{1}H; (*ii*) its resonance differs by only 6% from that of ^{1}H, potentially

allowing ^{19}F-MRI to be conducted on existing ^{1}H imaging hardware; (*iii*) an extremely broad chemical shift range and T_1 sensitivity to oxygen tension that can permit its use as an in vivo sensor; (*iv*) it is not naturally present in biological tissues and therefore does not contribute to background signal (solid fluorides in bones and teeth have very short T_2 values, and thus do not increase background noise) [17]. As a consequence of this last property of fluorine, there is no detectable background signal in tissues, and the ^{19}F-MRI signal comes only from the fluorinated CAs injected in the body (**Fig. 4)** [15]. The most commonly used ^{19}F-MRI probes are perfluorocarbons.

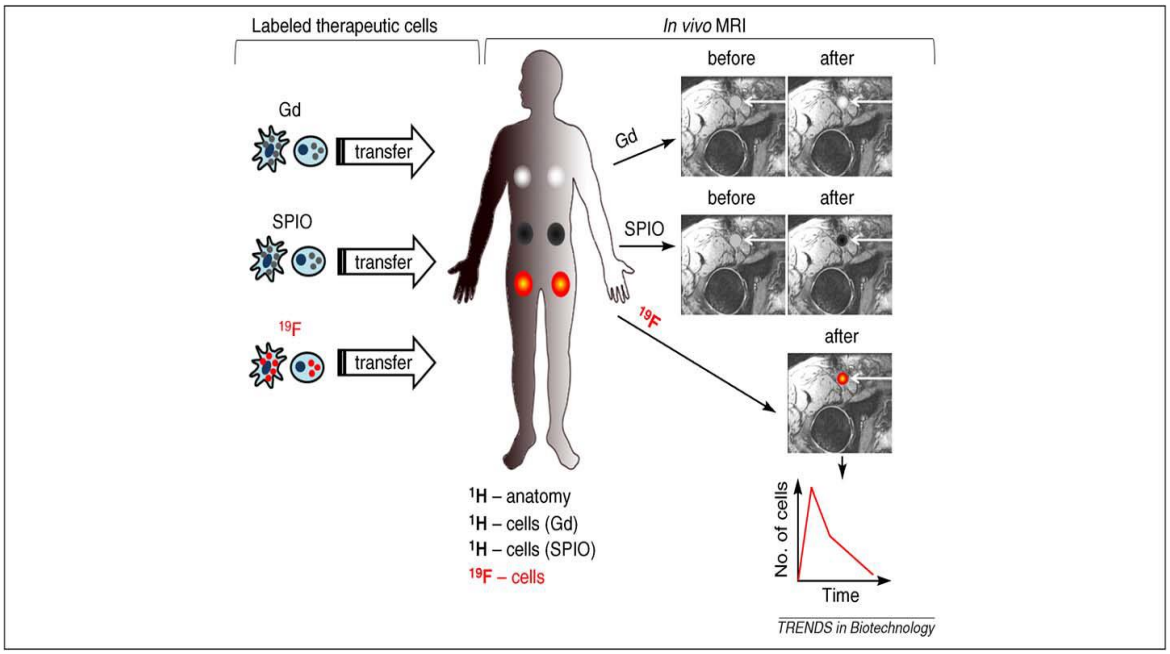

Figure 4. Gd and SPIO labels typically require 'before' and 'after' images for localization (white arrows), resulting in a final hyperintense or hypointense spot signal, respectively. With a ^{19}F label, imaging can be carried out in a longitudinal manner for ^{19}F (specifically the labeled cells) and ^{1}H (anatomy) without a 'before' image. Furthermore, the total ^{19}F signal can be calculated from the in vivo data, providing tracking information for both the localization and number of cells. Such quantitative, unambiguous cell tracking is not possible using standard imaging techniques in conjunction with metal-based contrast agents. [15].

1.3 Perfluorocarbons as ^{19}F-MRI tracers

Perfluorocarbons (PFCs) are organic compounds in which all hydrogen atoms bound to carbon are replaced with fluorine. They are characterized by excellent chemical and biological inertness, and intense hydrophobic and lipophobic effects. These unique properties of PFCs can be attributed to the high electronegativity and increased size of fluorine atom compared to hydrogen one, and to the strength of the C-F bond which is the strongest existing covalent bond. Thanks to the properties described above, PFCs have been studied and used as 'tracers' for imaging. They are not degraded at physiological pH values, they are generally not metabolized by enzymes and they tend to be disposed of by the reticuloendothelial system and expelled through the lungs by exhalation. As a result, these molecules tend to be more stable than the non-fluorinated CAs used for proton-based MRI, and their toxicity is reduced [18]. The MRI performance of a fluorinated tracing agent is strictly affected by its chemical structure. In particular, the essential characteristics that a suitable fluorinated MRI probe should possess are: (*i*) high fluorine content, (*ii*) easy synthesis and formulation in water, (*iii*) definite chemical properties, (*iv*) chemical and biological stability, possibly with a long shelf-life, (*v*) low in vitro and in vivo toxicity, (*vi*) simple ^{19}F-NMR spectrum (*vii*) short T_1 and long T_2 [16]. The most studied PFCs as tracers for ^{19}F-MRI are listed in **Fig. 5.**

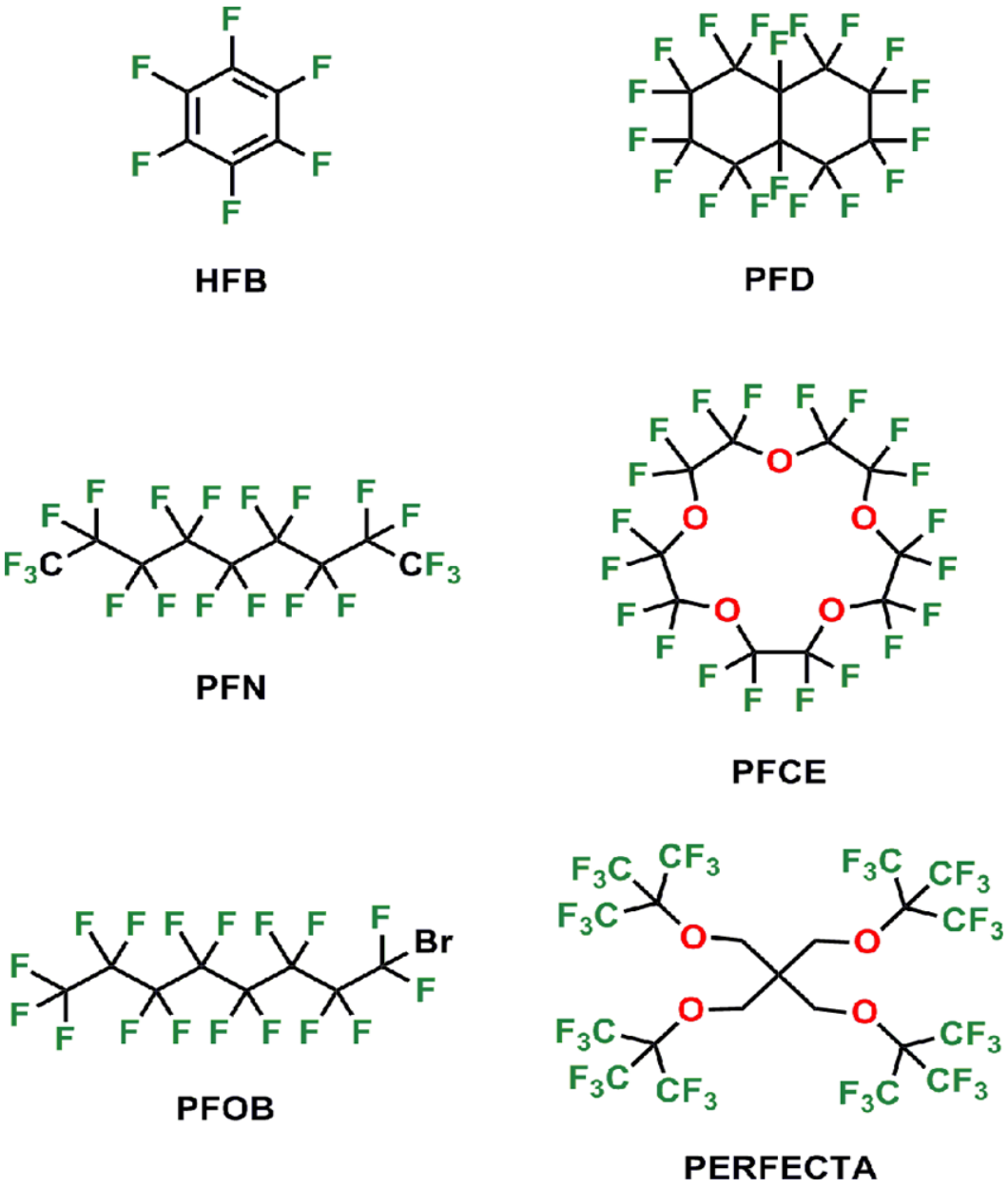

Figure 5. Chemical structures of some ^{19}F MRI molecular tracers: hexafluorobenzene (HFB), perfluorodecalin (PFD), perfluorononane (PFN), perfluoroctyl bromide (PFOB), perfluoro-15-crown-5-ether (PFCE) and PERFECTA. [16].

Hexafluorobenzene (HFB) is a small fluorinated molecule that exhibits exceptional in vivo sensitivity to changes in oxygen tension. When administered, in central and peripheral regions of rat breast tumors, oxygen tension maps were achieved, and the correlation between tumor vascular oxygenation and tissue oxygen tension dynamics was investigated [19]. Perfluorodecalin (PFD) is widely

used as a blood substitute and for liquid-assisted ventilation, it is an alternative and nontoxic PFC for in vivo inflammation imaging, although very weak signal intensities were obtained [20]. Perfluorononane (PFN) proved to be a well-tolerated and biologically inert oral CAs for in vivo gastrointestinal imaging [21]. Perfluorooctyl bromide (PFOB) is a hydrophobic and dense liquid, has a low diffusion coefficient into blood, and displays an enhanced clearance rate from the body due to the presence of bromine and it possesses minimal toxicological risks, since it is extremely inert and stable [22]. However, all these CAs have a nonequivalent distribution of fluorines, which generates a multipeak resonance spectrum, creating chemical shift artifacts with replicated images [16]. Moreover linear-chain PFCs with more than six CF_2 units are candidates for a new class of persistent organic pollutants, organic compounds which remain intact in the environment for long periods. The strength of the carbon–fluorine bond renders PFCs resistant to degradation, hydrolysis, photolysis, and metabolism by vertebrates, and increases their tendency to accumulate in humans and animals, with suspected long-term toxicity [23]. For these reasons, linear chain PFCs with more than six CF_2 units were recently banned. This pushed research effort towards the development of less harmful, but similarly performing fluorinated compounds, mainly focusing on shorter PFC chains (less than four carbon atoms) or branched chains, whose lower lipophobicity is expected to reduce bioaccumulation [24]. A good alternative to PFOB is given by perfluoro-15-crown-5-ether (PFCE). Thanks to its 20 chemically equivalent fluorine atoms, PFCE gives one ^{19}F MRI peak that makes it a suitable tracer for cell tracking and targeted drug delivery purposes [25]. Unfortunately all of these PFCs due to their hydrophobicity are insoluble in water. The most widely used strategy to overcome the poor water solubility of PFCs is to formulate PFC into oil-in-water (o/w) nanoemulsions. Usually such colloidal systems consist of nanodroplets with a PFC core coated by a lipid layer (**Fig. 6**) and can be stabilized by different emulsifiers. These agents reduce the surface energy and form a structural−mechanical barrier around PFCs particles, preventing them from sticking together.

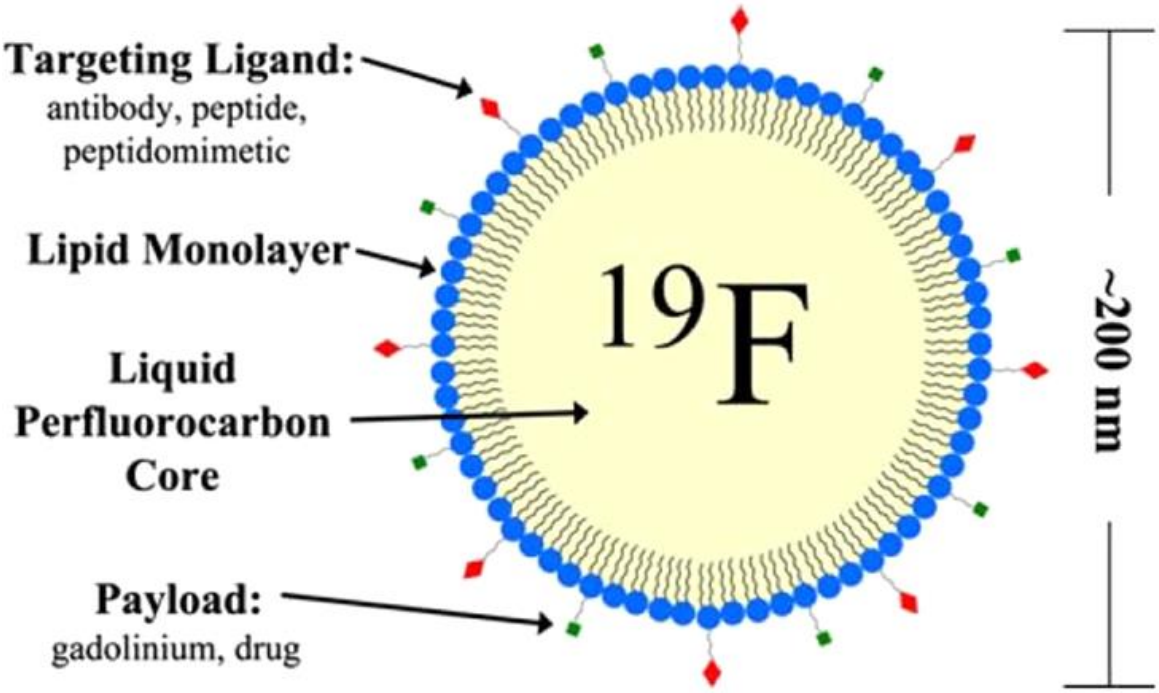

Figure 6. Cartoon representing a multifunctional PFC nanoemulsion droplet. The PFC core is coated by a lipid monolayer which can be functionalized with specific targeting and payload molecules. [16].

Unfortunately, PFCE is characterized by a relatively small fluorine content, its T_1 and T_2 values are largely influenced by tissue oxygenation, and its molecular structure cannot be further functionalized without dramatically altering its MRI or biological performances [16]. In order to overcome these issues and to develop a small molecule containing as many equivalent ^{19}F atoms as possible, a new superfluorinated molecular probe called PERFECTA (suPERFluorinatEd ContrasT Agent) has recently been designed, **Fig. 5**. PERFECTA was obtained in a single step via a Mitsunobu reaction between pentaerythritol and perfluoro-*t*-butanol. Differently from common PFC contrast agents, this molecule is not a perfuorinated compound because it has a hydrocarbon polar core completely screened by 36 equivalent ^{19}F external atoms. Moreover, the four ether bonds might favour its enzymatic degradation in vivo avoiding accumulation, even if there are no studies at the moment that guarantee its non-toxicity. PERFECTA

appears as a crystalline white powder insoluble in water and in most organic solvents (e.g., acetone, chloroform, methanol). However, it is possible to obtain a homogeneous emulsion with three different methods. The first method consists in dispersing a certain amount of PERFECTA in an aqueous solution of lecithin and safflower oil, obtaining an emulsion that is stable for weeks at room temperature. This emulsion, characterized by ^{19}F-NMR, shows a sharp, very intense single peak at −73.48 ppm with a concentration of PERFECTA of 74.40 mM, which corresponds to (1.61 ± 0.04) × 10^{21} ^{19}F atoms per mL of emulsion. DLS experiments figure out monodisperse samples, in several fluids (water, PBS, cell culture media with or without fetal bovine serum and human plasma) revealing high stability in all tested solutions with an averaged droplet size ranging between 140 and 220 nm. Moreover, its relaxation time, signal-to-noise ratio and its compatibility with cellular viability for long incubation periods up to 8h make PERFECTA a suitable contrast agent for ^{19}F-MRI applications [26]. The other two method are based on the synthesis of PERFECTA nanoparticles (NPs). PERFECTA NPs encapsulated with a combination of poly(lactide-co-glycolide) (PLGA), a biodegradable and biocompatible polymer used in drug delivery, and PFCE to increase encapsulation yield generating a fractal sphere structure. This “two color” MRI probe is reported to be biocompatible, suitable for in vivo imaging and with structural properties that potentially enable tracking of biodistribution and degradation, opening the way for future drug delivery and release studies [27]. The last method consists on NPs dispersion using a non-ionic surfactant, Pluronic F68, to obtain an emulsion in water that is stable for weeks at room temperature [28]. PERFECTA seems to have all the characteristics that make it a suitable ^{19}F MRI tracer, whose only drawback is its insolubility in water. Hence, before in vivo application, this molecule need to be emulsified. These emulsions required time for formulation and the use of organic solvents that have to be disposed of. A highly fluorinated tracer soluble in water can be worthwhile in terms of time and pollution with respect to PERFECTA. A possible candidate with the characteristics mentioned before can be a fluorinated ionic compound; in particular this thesis’ work will focus on tetrakis[perfluoro-tert-butoxy]aluminate

lithium salt, $Li[Al(OC(CF_3)_3)_4]$, whose anion $[Al(OC(CF_3)_3)_4]^-$ belongs to the category of weakly coordinating anions (WCAs) [29].

1.4 Fluorinated Alkoxyalluminates

The main feature of WCAs is the absence of strong cation–anion electrostatic interactions typical of classical salts, which are replaced by a multitude of weak interactions. In order to fulfil this purpose, WCAs should be large and exhibit diameters in the nanometer range. Moreover, their surfaces are often covered by poorly polarizable fluorine atoms that reduce the efficiency of ion pairing and increase the inertness and stability of these anions against ligand coordination or abstraction, as well as oxidation. Overall, this leads to an improvement of the solubility of WCA salts in less or even nonpolar solvents, reducing ion pairing in these solvents, and also leading to electric conductivity in these media. These WCAs are built from a very Lewis acidic central atom M that usually bears a range of mainly univalent, fluorinated ligands L giving the normally univalent ate-complexes $[M(L_{n+1})]^-$ (n = valency of M) as WCAs [30]. Among WCAs, fluorinated alkoxyaluminates $[Al(OR^F)_4]^-$ (with $R^F = C(CF_3)_3$ or other fluorinated organic residues) were first published by Strauss in 1996 and further developed by Krossing research group since 1999. The synthesis of purified and finely ground tetrakis[perfluorotert-butoxy]aluminate ($Li[Al(OC(CF_3)_3)_4]$) in 95% yield was achieved by the reaction between $LiAlH_4$ and commercially available perfluorinated tert-butyl alcohol (**equation 2**).

$$LiAlH_4 + 4\ HOR^F \longrightarrow Li^+ + [Al(OR^F]^- + 4\ H_2 \quad \text{with } OR^F = OC(CF_3)_3 \qquad \textbf{Eq.2}$$

The melting temperature of $Li[Al(OC(CF_3)_3)_4]$ is around 93°C as shown in **Fig. 7**

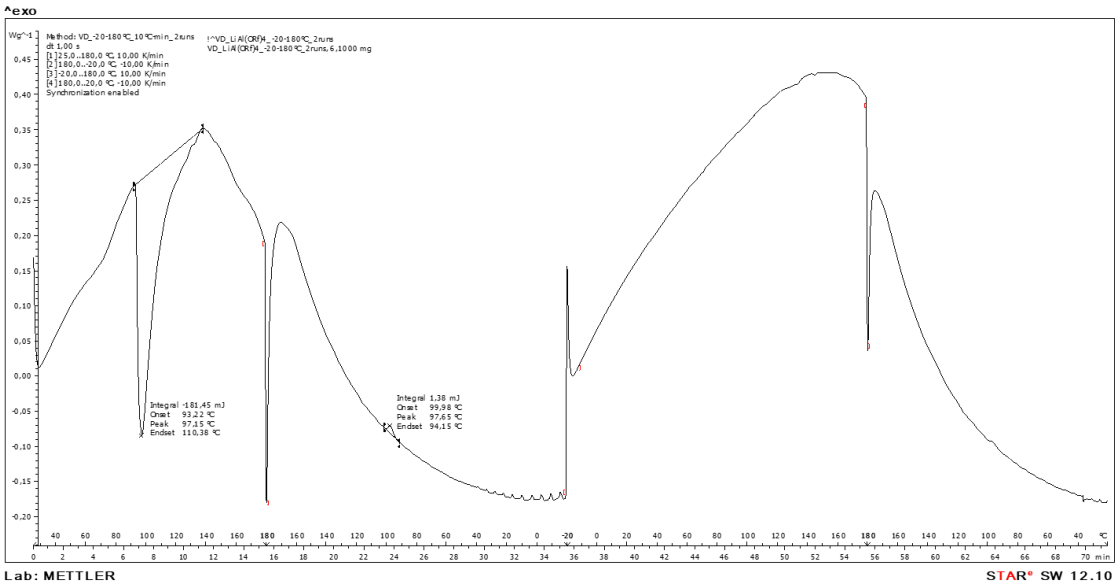

Figure 7: DSC thermogram of LiAl(ORf)4 (25 °C → 180 °C → -20 °C → 180 °C → -20 °C; heating rate: 10 °C/min) showing its melting transition at 93°C.

An approach to compare the coordinative abilities of anions and their weakly coordinating character is to visualize their electrostatic potential on a 0.025 e^- $Bohr^{-3}$ isodensity surface. The color coding of the surface area allows to understand which sections of the anion are coordinating (red=negatively charged), noncoordinating (yellow/green), or repulsive towards a cation (blue=positively charged), **Fig. 8**. From the representations collected in the figure below it is possible to realize that the classical small "WCAs" accumulate more negatively charged surface areas, whereas the more advanced ones, such as the alkoxyaluminate $[Al(OR^F)_4]^-$ (where oxygen atoms are shielded by the perfluorinated groups), are good candidates of almost noncoordinating anions [31].

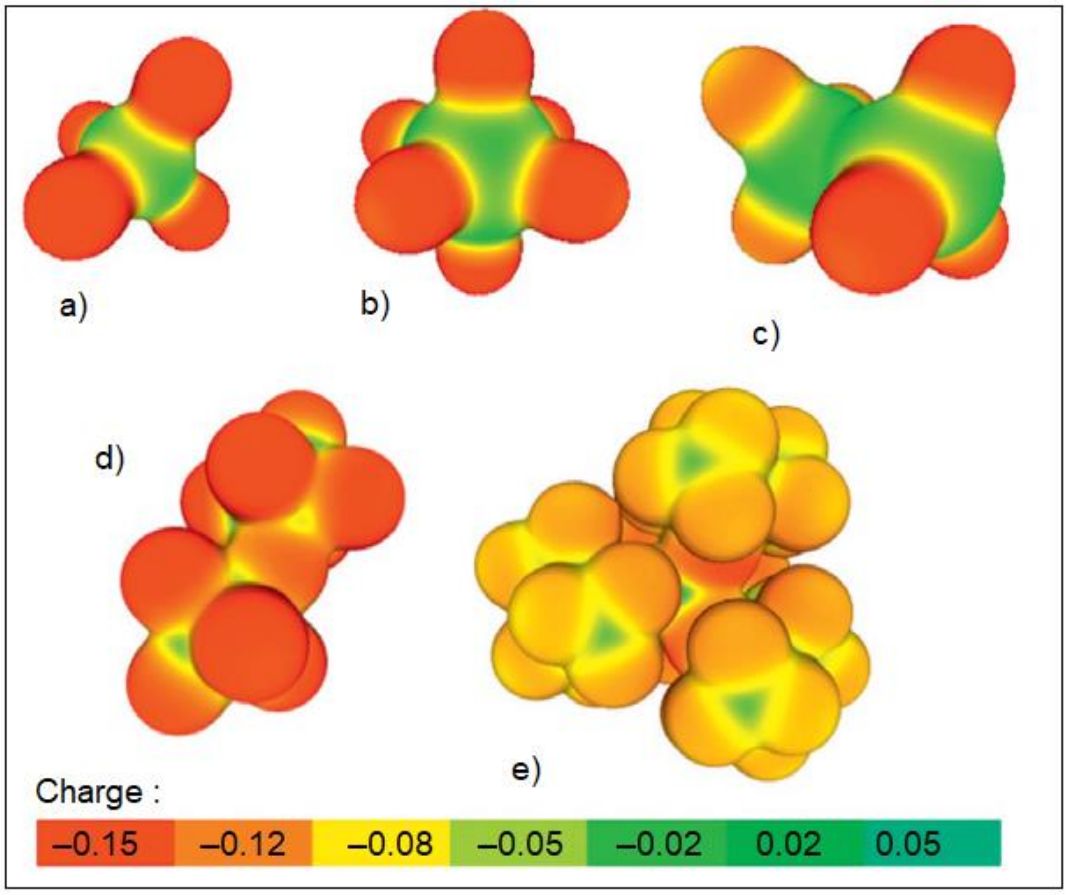

Figure 8. Projection of the PBE0/TZVPP-calculated electrostatic potential onto a 0.005 e^- $Bohr^{-3}$ isodensity surface of $[Al(OC(CF_3)_3)_4]^-$ in comparison to classical WCAs; a) $[BF_4]^-$, b) $[PF^6]^-$, c) $[F_3C–SO_3]^-$, d) $[Sb_2F_{11}]^-$, e) $[Al(OC(CF_3)_3)_4]^-$ [31].

The thermodynamic stability of these WCAs was established based on the following considerations:

(i) The fluoride ion affinity (FIA). All anions that are based on Lewis acidic central atoms are subjected to ligand abstraction as a decomposition reaction. The higher the FIA value of the parent Lewis acid, the more stable is the WCA against ligand abstraction.

(ii) The energy of the highest occupied molecular orbital (HOMO) of a WCA relates to its resistance toward oxidation. The lower the HOMO energy, the more difficult it is to remove an electron and thus to oxidize the WCA.

(iii) The HOMO–lowest unoccupied molecular orbital (LUMO) gap can be associated with the resistance of an anion toward reduction and the larger the gap, the more stable is the anion with respect to reduction. Very small gaps are an indication of the potentially oxidizing character of these anions that may interfere with counter-cations sensitive toward oxidation [32].

The properties of WCAs analyzed so far have allowed their application in different fields, including their application in catalysis, their use as supporting electrolytes, in ionic liquids, and in biological applications, as briefly detailed below.

1.4.1 Applications in Catalysis and Polymerization Chemistry

Weakly coordinating anions (WCAs) have been applied extensively in catalysis during the last decade, due to the fact that WCAs have a stabilizing effect on the cations that support the creation of a vacant coordination site on metal centres, rendering the intermediate species more accessible to substrate coordination. The applications of WCAs include polymerization reactions, as well as various organic transformations. From a very general point of view, good WCAs like the aluminates $[Al(OR^F)_4]^-$ should be employed, if the catalysis/polymerization under investigation presents difficulties with classical ions, such as $[CF_3SO_3]^-$, $[BF_4]^-$,or $[PF_6]^-$ ·If the catalysis runs already very well, there is no need to introduce a good WCA. However, if one of the limiting situations shown in **Fig. 9** plays a negative role, one should definitely consider employing a catalyst partnered with a good WCA. Besides reduced ion pairing, especially the greatly improved solubility of WCA catalysts in low polarity, noncoordinating solvents can be used to increase the overall catalyst activity and selectivity [30].

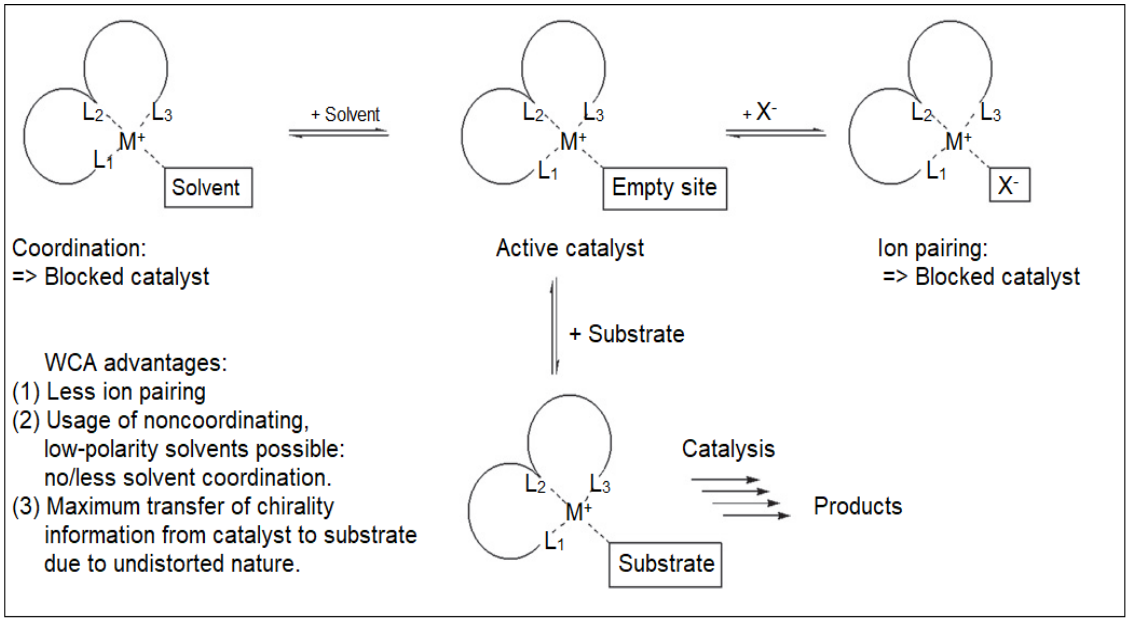

Figure 9. How ion pairing and solvent coordination may block catalysis. Both effects may be improved by using good aluminate $[Al(ORF)4]^-$ based WCAs. [30].

1.4.2 Supporting electrolytes

The use of WCAs as a supporting electrolytes has a significant advantage over the use of traditional smaller anions, as they have greater solubility and dissociation, and therefore conductivity, in low-polarity solvents. Electrolytes containing WCAs can also be applied to study the electrochemistry of multiply charged complexes, as the species formed maintain their solubility and show a reduced tendency to be deposited on the electrode. Moreover, the reduced levels of ion pairing from WCAs allow the separation of oxidation events [31].

1.4.3 Ionic liquids

By definition, ionic liquids are salts that contain organic cations and inorganic or organic anions and have a melting point below 100 °C. Weakly coordinating anions recently became more and more important for ionic liquids (ILs) because they show a much lower tendency to coordinate cations if compared to halide counterions. Due to the weaker interactions between the cation and the bulky WCA, the properties of ILs like melting point, viscosity, thermal stability, or acidity can be modified [32].

1.4.4 Biological applications

Dye-loaded polymer nanoparticles (NPs), due to their high brightness and potential biodegradability, are a powerful alternative to quantum dots in bioimaging applications. To minimize aggregation-caused quenching of the loaded dyes, Andreiuk et al. have recently proposed the use of cationic dyes with bulky hydrophobic counteranions, instead of the most used tetrakis(pentafluorophenyl)borate: F5-TPB, which serve as spacers preventing dye π-stacking inside nanoparticles, **Fig. 10a**. This study showed that the $Al[OC(CF_3)_3]_4^-$ anion strongly improved the encapsulation efficiency of octadecyl-rhodamine B dye inside NPs made of the biodegradable PLGA, even at 50 mM dye loading with respect to F5-TPB **Fig. 10b.** According to single-particle microscopy, the obtained NPs are 33-fold brighter than commercial quantum dots QD585 at 532 nm excitation and exhibit complete ON/OFF switching (blinking) due to the collective behaviour of the dyes inside the polymer matrix**.** [33].

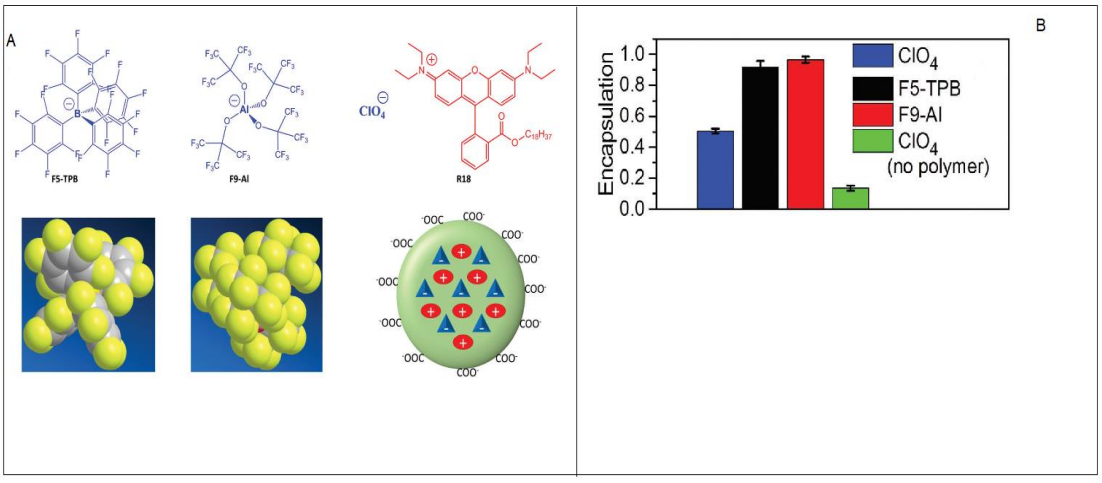

Figure 10. (A) Chemical structures and molecular models of counterions used to encapsulate octadecyl-rhodamine B dye (R18) inside polymer nanoparticles; (B) encapsulation efficiency. Adapted from [33].

1.5 Aim of the thesis

The structure of the $[Al(OC(CF_3)_3)_4]^-$ anion (that from the following chapter will be indicated as $^-AlR^F$) recalls the PERFECTA one, since both have 36 equivalent fluorine atoms, as shown in **Fig. 5**. Such structural similarity suggested the hypothesis that it may have all the outstanding characteristics that make the PERFECTA a good contrast agent for fluorine-based MRI. Moreover, its negative charge could be able to overcome the high degree of fluorination, making it enough soluble in water, without requiring the use of surfactants or emulsifiers as in the case of PERFECTA. The present thesis work aimed to establish the best conditions for maximizing the solubility of $LiAlR^F$ in water in view of its possible use as ^{19}F-MRI probe.

Chapter 2: Materials and Methods

2.1 Materials

For this work, a sample of $LiAlR^F$ (MW: 973,98 g/mol) kindly provided by Prof. I. Krossing (University of Freiburg, Germany) was used and dissolved in Milli-Q water under different conditions. Milli-Q water (mQw, 18.2 mΩ/cm) was obtained by the purification system provided by Simplicity®. For ^{19}F NMR quantifications, a solution of trifluoroacetic acid (TFA) in deuterium oxide (D_2O) was used as external standard. Both reagents were purchased from Sigma-Aldrich.

2.2 Methods

In order to increase the solubility of the salt, different instruments were used: a sonicator bath at 59 KHz; a tip sonicator (130 W, 20 kHz) and a magnetic stirrer. The resulting samples have been characterized in terms of ^{19}F-NMR performance and stability over time, whereas particles size distribution was characterized mainly through Dynamic Light Scattering (DLS).

DLS analyses were performed at ALV compact goniometer system, equipped with ALV-5000/EPP Correlator, special optical fiber detector and ALV/GCS-3 Compact goniometer, with He-Ne laser (λ = 633 nm, 22 mW output power) as light source. The temperature was controlled with a thermostatic bath and set at 25°C. A sample volume of 1 mL was used for the analysis. DLS was measured at different time points (0, 1, 6, 7 days) and scattering angles θ = 70 – 130° in 20° steps. Each measurement was the result of the average of three subsequent run of 10 seconds each, with a threshold sensibility of 10%. Data analysis was done with ALV-Correlator software. The apparent hydrodynamic radii at different angles were obtained from an intensity weighted and a number weighted fitting of the autocorrelation function. ^{19}F-NMR spectra reported in this thesis were registered on Bruker AV400 spectrometer, operating at 380 MHz for the ^{19}F nucleus. Samples were prepared filling the probe tube with 400 µL of the starting

solution and using as external reference 100 µL of a solution of trifluoroacetic acid (TFA) in D_2O, that has a concentration of $3.43x10^{18}$ ^{19}F atoms/mL. Transmission Electron Microscopy (TEM) images were acquired by using a DeLong America LVEM5, equipped with a field emission gun and operating at 5 kV. Samples were prepared by placing 10 µL of sample solution on 200 mesh carbon-coated copper grids, leaving the water evaporate from the surface of the grid. Thermal analysis and melting point measurements were performed using a Mettler Toledo DSC 823e differential scanning calorimeter. The following sections present a more detailed description of the main experimental techniques used during this thesis work.

2.2.1 Dynamic Light Scattering

Dynamic light scattering (DLS) is based on the Brownian motion of particles dispersed in a liquid, which move randomly in all directions. The principle of Brownian motion is that particles are constantly colliding with solvent molecules. These collisions cause a certain amount of energy to be transferred, which induces particle movement. The energy transfer is more or less constant and therefore has a greater effect on smaller particles. As a result, smaller particles are moving at higher speeds than larger particles. Knowing all the parameters that influence particle movement, it is possible to determine the hydrodynamic diameter by measuring the speed of the particles. The relation between the speed of the particles and their size is given by the Stokes-Einstein equation (**equation 3**). The speed of the particles is given by the translational diffusion coefficient *D*. Further, the equation includes the viscosity of the dispersant and the temperature because both parameters directly influence particle movement.

$$\mathrm{D} = \frac{K_B T}{6\pi\eta\mathrm{RH}} \qquad \textbf{Eq.3}$$

D Translational diffusion coefficient [m²/s] – “speed of the particles”

k_B Boltzmann constant [m²kg/Ks²]

T Temperature [K]

η Viscosity [Pa.s]

R_H Hydrodynamic radius [m]

A basic requirement for applying the Stokes-Einstein equation is that the movement of the particles have to be caused by Brownian motion. Sedimentation suppresses random movement, and would lead to inaccurate results. Therefore, the onset of sedimentation indicates the upper size limit for DLS measurements. In contrast, the lower size limit is defined by the signal-to-noise ratio. Small particles do not scatter much light, which leads to an insufficient measurement signal. The basic setup of a DLS instrument is shown in **Fig. 11a**. A single frequency laser is directed to the sample contained in a cuvette. If there are particles in the sample, the incident laser light gets scattered in all directions. The scattered light is detected at a certain angle over time and this signal is used to determine the diffusion coefficient and the particle size by the Stokes-Einstein equation. The incident laser light is usually attenuated by a gray filter, which is placed between the laser and the cuvette. The filter settings are either automatically adjusted by the instrument or can be set manually by the user. When turbid samples are measured the detector would not be able to process the amount of photons. Therefore, the laser light is attenuated to receive a sufficient but processable signal at the detector. The intensity of the scattered light is not constant, but will fluctuate over time and is detected over a certain time period in order to monitor the movement of the particles. Smaller particles, which are moving at higher speeds, show faster fluctuations than larger particles. On the other hand, larger particles result in higher amplitudes between the maximum and minimum scattering intensities, as shown in **Fig. 11b**. This initial intensity trace is further used to generate a correlation function. In general, the correlation function describes how long a particle is located at the same spot within the sample. At the beginning, the correlation function has an upper plateau, indicating that the particle is still at the same position as it was the moment before. Later, an exponential decay of the correlation function can be observed, meaning that the particle is moving. If there is no similarity to the initial spot, the correlation function shows a lower plateau, this part of the correlation function is known as

the baseline. Information about the size-dependent movement is included in the decay of the correlation function. The decay represents an indirect measure of the time that the particles need to change their relative positions. Small particles move quickly so the decay is faster. Larger particles move more slowly and therefore the decay of the correlation function is delayed [34].

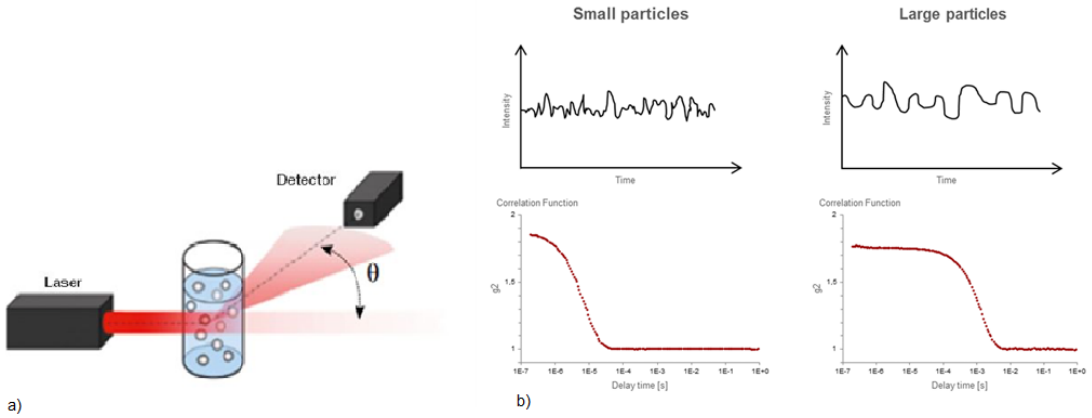

Figure 11: a) Basic setup of a DLS measurement system. The sample is contained in a cuvette. The scattered light of the incident laser can be detected at different angles; b) Differences in the intensity trace and correlation function of large and small particles. Smaller particles show faster fluctuations of the scattered light and a faster decay of the correlation function [35].

Indeed, the correlation function is a mathematical description of the fluctuations of the scattered light. It is used to determine the translational diffusion coefficient. To do this, the intensity of the scattered light at a time t is compared with the intensity of the same intensity trace shifted by the delay time τ (tau). Different delay times are marked by a different color. Each single value of the normalized time correlation function $g2$ is then obtained by adding together the product of two values at the same time of these two intensity traces. Doing this for different delay times results in the desired correlation function. These calculations are done in real time and plotted over a logarithmic time axis. Cumulant algorithms are used in order to fit the correlation function, which is an ISO-standardized procedure. The diffusion coefficient is determined from the cumulant algorithm; the hydrodynamic diameter (i.e. particle size) is further obtained by the already

discussed Stokes-Einstein equation. As described above, the particle size of the sample is not measured directly but is based on the movement of the particles. The term hydrodynamic diameter refers to the particle size of smooth, spherical particles which diffuse at the same speed as the particles of the sample. The polydispersity index (PDI) is given in order to describe the broadness of the particle size distribution. The polydispersity index is also calculated by the cumulant method. A value below 10 % reflects a monodisperse sample and indicates that all of the measured particles have almost the same size. However, the polydispersity index does not provide any information about the shape of the size distribution or the ratio between two particle fractions. As the results of DLS measurements are intensity-based (the intensity fluctuations over time are detected) this is the primary weighting model displayed in a DLS software. The intensity-based distribution can be re-calculated to a volume- and number-based distribution. For this, the material refractive index and the absorbance of the measured sample at the wavelength of the laser need to be known. Intensity-based techniques show an emphasis on larger particles (they scatter more light than smaller particles). Volume- and number-based distributions will show a tendency to smaller particle fractions. It is important to note that all three-size distributions are just different representations of the same physical reality of a distribution of differently sized particles [35].

2.2.2 Nuclear Magnetic Resonance Spectroscopy

Over the past fifty years, Nuclear Magnetic Resonance spectroscopy, commonly referred to as NMR, has become a fundamental technique for determining the structure of organic compounds. NMR is a non-destructive analytical technique, and with modern instruments good data may be obtained from samples weighing less than one milligram. The nuclei of many elemental isotopes have a characteristic spin (**I**). Some nuclei have integer spins (e.g. I = 1, 2, 3, …), some have fractional spins (e.g. I = 1/2, 3/2, 5/2, …), and a few have no spin, I = 0 (e.g. ^{12}C, ^{16}O, ^{32}S). Isotopes of particular interest to organic chemists

are ^{1}H, ^{13}C, ^{19}F and ^{31}P, all of which have I = 1/2[38]. The following events lead to the NMR signals**:**

1. A spinning charge generates a magnetic field, (**fig. 12a)**. The resulting spin-magnet has a magnetic moment (**μ**) proportional to the spin.

2. In the presence of an external magnetic field ($\mathbf{B_0}$), two spin states exist, **+1/2** and **-1/2**.
The magnetic moment of the lower energy +1/2 state is aligned with the external field, whereas that of the higher energy -1/2 spin state is opposed to the external field. **(Fig. 12b)**.

3. The difference in energy between the two spin states is dependent on the external magnetic field strength, and is always very small. **Fig.10c** illustrates that the two spin states have the same energy when the external field is zero, but diverge as the field increases. At a field equal to B_x, the energy difference is given by the formula reported in the graph (where I = 1/2 and μ is the magnetic moment of the nucleus in the field) [36].

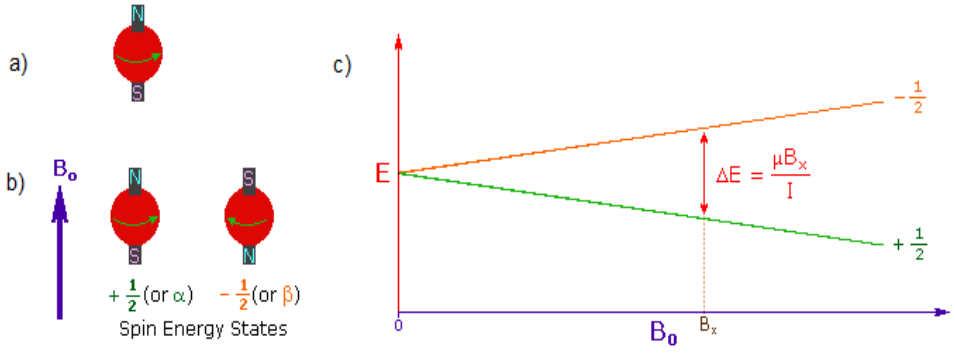

Figure 12: a) A spinning charge generates a magnetic field; b) In the presence of an external magnetic field ($\mathbf{B_0}$), two spin states exist, **+1/2** and **-1/2**; c) The difference in energy between the two spin states. [37].

To begin with, the NMR spectrometer must be tuned to a specific nucleus, in this case the proton. The actual procedure for obtaining the spectrum varies, but the simplest is referred to as the continuous wave (CW) method. A typical CW-

spectrometer is shown in **Fig. 13**. A solution of the sample in a 5 mm-diameter glass tube is oriented between the poles of a powerful magnet, and is spun to average any magnetic field variations, as well as tube imperfections. Radio frequency (RF) radiation of appropriate energy is broadcast into the sample from an antenna coil (shown in red in the Figure). A receiver coil surrounds the sample tube, and emission of absorbed RF energy is monitored by dedicated electronic devices and a computer. A NMR spectrum is acquired by varying or sweeping the magnetic field over a small range while observing the RF signal from the sample. An equally effective technique is to vary the frequency of the RF radiation while holding the external field constant. Strong magnetic fields are necessary for NMR spectroscopy, ranging from 1 to 20 T. For NMR purposes the energy difference (ΔE) between the two spin states is usually given as a frequency in units of MHz (106 Hz), ranging from 20 to 900 Mz, depending on the magnetic field strength and the specific nucleus being studied. Irradiation of a sample with RF energy corresponding exactly to the spin state separation of a specific set of nuclei will cause excitation of those nuclei in the +1/2 state to the higher -1/2 spin state. NMR spectroscopy is therefore the energetically mildest probe used to examine the structure of molecules.

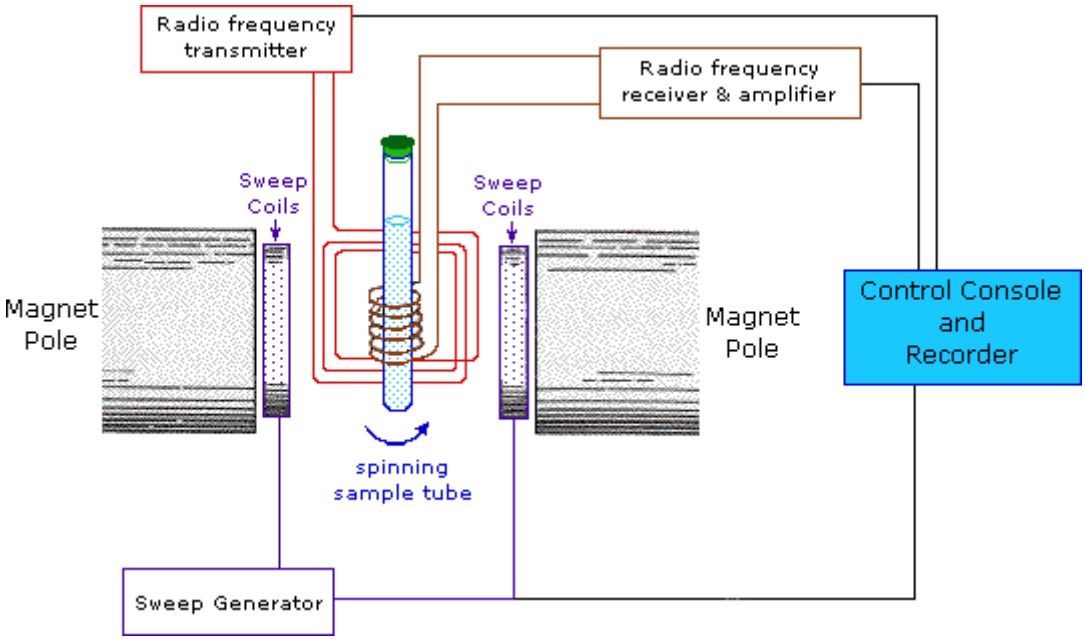

Figure 13. A typical CW-spectrometer [37].

The key parameter in NMR experiments is the chemical shift that expresses the variation of resonance frequency due to the electron cloud. In fact, the magnetic field felt by the nucleus is altered by the presence of electrons that can act as a “shield" expressed by σ (generally positive). Therefore, the actual resonance frequency is (**equation 4**):

$f = \frac{\gamma B_0(1-\sigma)}{2\pi}$ γ = gyromagnetic ratio **Eq.4**

Due to this shielding effect, for example, the presence of electron-withdrawing groups in the molecule reduces the electron density around the nucleus, shifting its resonance frequency to higher values, and vice versa. Furthermore, the resonance can also be altered by the other nuclei nearby. The influence of neighbouring spins causes a splitting of peaks in the spectrum, in a process called spin-spin splitting. The distance between the peaks indicates how strongly the nuclear spins interact with each other. This coupling arises because information about nuclear spin is transferred via electrons along the bond between the nuclei as stated by Fermi contact mechanism. The complexity of the spectrum, therefore, increases as the number of neighbouring spins increases and because, it is important to understand molecular parameters such as bond strengths and steric arrangements. Coupling between nuclei that have the same chemical shift (chemically equivalent) and nuclei that are more than three bonds away do not lead to splitting in the spectrum [36]**.**

2.2.3 Transmission Electron Microscopy

A transmission electron microscope (TEM) operates by accelerating a beam of electrons to a sufficient energy so that when incident on a very thin sample (<100 nm), electrons are transmitted through it. Conventional TEMs work on the same principle as light microscopes, but use a beam of electrons, which travels in vacuum and is originated by an electron gun source, rather than a light source (see TEM optics in **Figure 14**). The first TEM was built by Ernst Ruska and Max Knoll in 1931 [38], with the first commercial TEM developed only four years later. The invention of TEM came about due to the limitations of using light for imaging

objects, as optical microscopes are constrained by the resolution and diffraction limits of the wavelengths of visible light. For any optical system, the theoretical diffraction resolution limit is given by Rayleigh's criterion, which describes the smallest resolvable distance between two points. The diffraction limit is proportional to the wavelength and therefore a straightforward approach to improve the resolution would be to use a source with a shorter wavelength, such as electrons. It is known from Louis de Broglie's work that electrons, while considered as particles, can also have wave-like properties. Therefore, increasing the momentum of an electron beam will decrease its wavelength, and as a result greatly increase the resolution limit over that attainable by visible light [39]. For a TEM operating with an accelerating voltage of 200 kV, the theoretical wavelength of the electrons will be ~2.51 pm, much smaller than the wavelength of visible light (550 nm for green light). Hence, the electron beam can reach a theoretical resolution limit smaller than atoms themselves. However, this theoretical resolution does not consider the aberrations, which are present in the optics of a TEM; the aberrations limit the resolution in TEM beyond this theoretical limit. The main components of the TEM are shown schematically, along with the corresponding ray diagram, in **Fig. 14**. The main components consist of: the electron gun (source of electrons); gun alignment controls; condenser lenses (magnetic lenses to collimate the beam); objective lens (to focus and initially magnify the image); apertures (to limit the diameter of the electron beam); intermediate lens; projective lens; sample holder; viewing screen and detectors to pick up the main and secondary signals. There are four main parameters, which determine the nature, and the quality of the image or spectrum obtained with a TEM, these are the probe size, convergent angle, electron energy and the electron probe current [40].

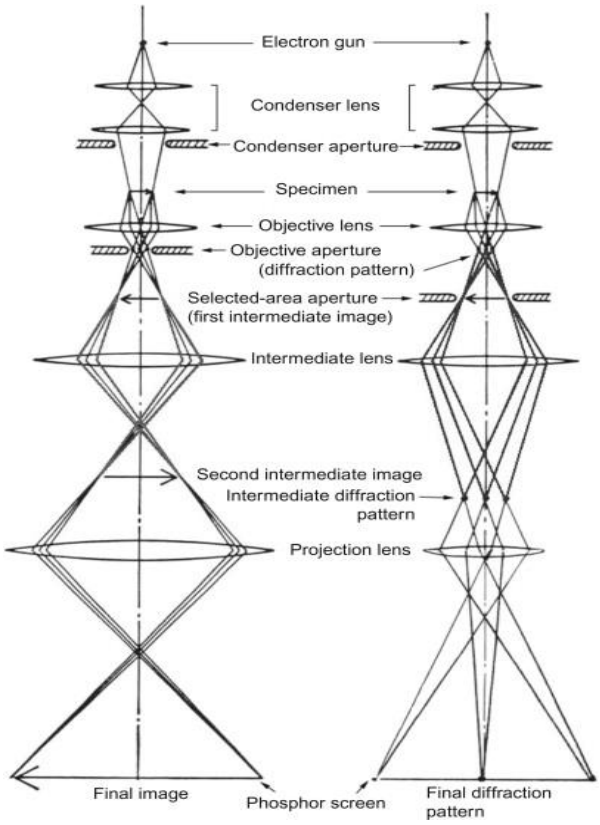

Figure 14: Schematic ray diagram of a conventional TEM microscope [40].

Chapter 3: Results and discussion

3.1 Water solubility

$LiAlR^F$ salt, as mentioned in chapter 1.4, can be dissolve in water. In a first attempt, 23 mg of salt were dissolved in 25 ml of MQ water (1 mM) and were sonicated for 5 minutes. The solution appeared cloudy with white fluctuating filaments and aggregates, is more like a dispersion, and after a few hours some white aggregates were visible at the bottom of the flask. Five more diluted solutions were then prepared with the same time of sonication, respectively 0.8 - 0.5 - 0.2 - 0.1 – 0.05 mM. After 3 hours, 1 ml of supernatant was withdrawn from each dispersion and analysed at DLS and NMR as described in chapter 2.2.1 and 2.2.2 The ^{19}F-NMR spectra showed a single, sharp peak at -75,20 ppm whose intensity decreased with concentration, and the peak of the 0.05 mM dispersion had a lot of background noise that made the ^{19}F-NMR quantification analysis problematic. The autocorrelation functions from DLS analysis showed the presence of aggregates, apart from the 0.05 mM dispersion, whose autocorrelation function was too noisy and flat for an appropriate analysis, which means that the sample was too diluted. The samples were left in the vials for one day at room temperature, and during this time aggregates started to deposit at the bottom, as shown in **Fig. 15.**

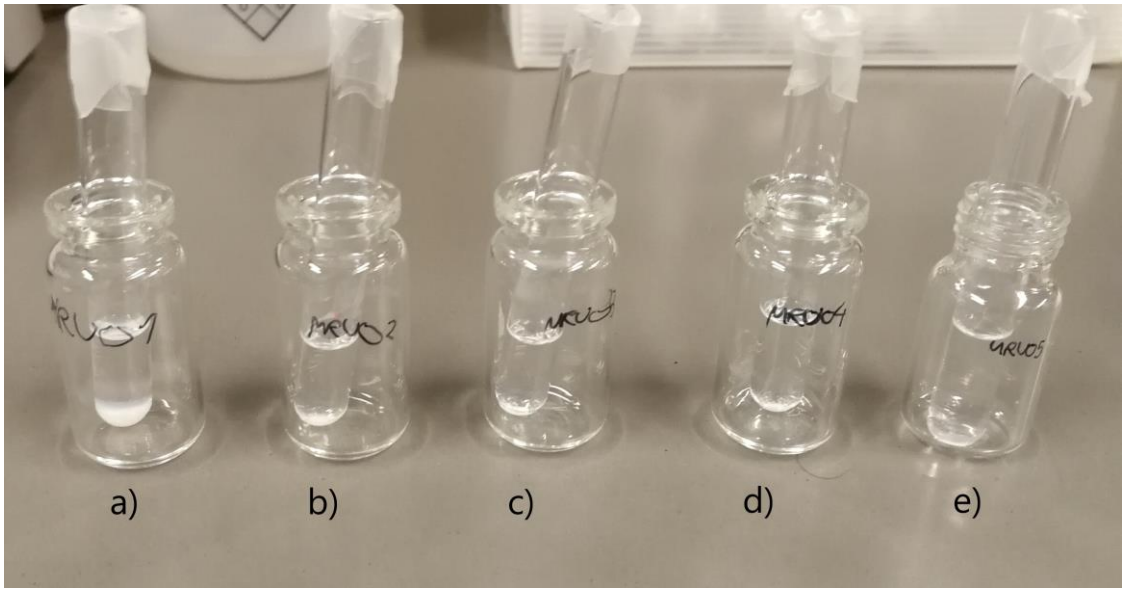

Figure 15: Picture showing the vials with LiAlR^F salt dissolved in MQ water at different concentrations, after one day of resting: a) 0.8, b) 0.5, c) 0.2, d) 0.1, e) 0.05 mM.

3.2 Screening of different dissolution methods

The previous experiments revealed that the dispersion of LiAlR^F with an estimated concentration of 0.1 mM could be the best compromise in order to have a detectable NMR signal for ^{19}F-NMR quantification and an analysable autocorrelation function. **Table 1** lists all the different methods performed on a 0.1 mM dispersion in order to figure out which was the best way to obtain the maximum concentration of LiAlR^F in water. Seven different experiments were carried out. In all cases, the dispersions were prepared starting from 1 mg of LiAlR^F weighted in a glass vial, to which 10 mL of MQ water were added. The first three were based on the same principle of mixing, magnetic stirring, with progressively increasing temperatures: room temperature, 50°C and 100°C (under reflux), which is above the melting temperature of the LiAlR^F (see **Fig. 7**). In the fourth experiment, mixing was still performed by magnetic stirring, but keeping the sample under an atmosphere of perfluorohexane vapors. According to previously reported studies [41], [42], indeed, perfluorocarbon gases (in particular, perfluorohexane) were able to stabilize phospholipid-coated and protein-coated microbubbles in aqueous media by osmotic effect and fluorous

interactions. We thus surmised if a similar stabilization effect could work on the perfluorinated anion of $LiAlR^F$, increasing its water solubility. In order to check this hypothesis, the sample was stirred while flushing it with a nitrogen flow saturated with perfluorohexane vapors. The last three experiments were performed at room temperature, but employing an ultrasound (US) bath and a tip sonicator, respectively, for mixing. The detailed procedures used for each trial sample are described below:

Table 1: List of all the dissolution methods tested to find the highest possible concentration of dissolved salt. Each sample had an estimated starting salt concentration of 0.1 mM.

Sample	Method
A	The vial was put in a thermostatic bath on a magnetic stirring plate; inside the vial a magnetic anchor rotated at 400 rpm for 17 hours. The temperature was kept at 25°C controlled by a thermometer.
B	The vial was put in a thermostatic bath on a magnetic stirring plate; inside the vial a magnetic anchor rotated at 400 rpm for 17 hours. The temperature was kept at 50°C by a digital thermometer probe.
C	The sample was refluxed under magnetic stirring for 2 hours.
D	The vial containing $LiAlR^F$ in water was connected in series with needles to three previous vials, each filled with 5 mL of liquid perfluorohexane, **Fig. 16**. Nitrogen was flushed starting from the headspace of the first perfluorohexane-containing vial for 30 minutes, in the meantime the dispersion was mixed with a magnetic anchor rotating at 400 rpm; then the nitrogen flux was interrupted and the mixing went on for 17 more hours.
E	The vial was put in the ultrasound bath for 10 minutes at 59 KHz, then it was left to rest for 2 minutes. This procedure was repeated three times; during the experiment the temperature of the US bath raised from 25°C to 33°C.
F	The vial was put in the ultrasound bath for 10 minutes at 59 KHz at 50°C, then 2 minutes of rest. This procedure was repeated three times; during the experiment the temperature of the US bath raised form 50°C to 56°C.
G	The vial was mixed with a tip sonicator (130 W, 20 kHz) operating at 80% of amplitude for 1 minute, followed by 5 minutes of rest; this procedure was repeated three times. To avoid excessive temperature increase and evaporation of the solvent, the vial was cooled into ice during sonication.

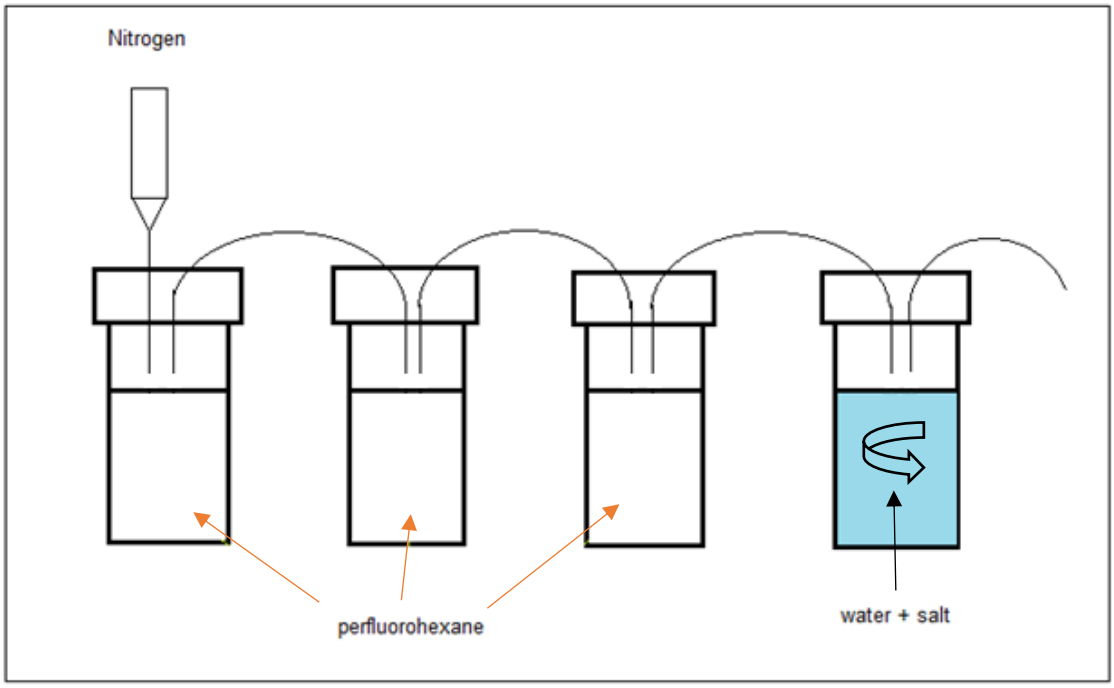

Figure 16: set up of sample D experiment; the last vial was magnetically stirred.

For all the methods described previously, the stability over time of the resulting LiAlR^{F} samples in water, in terms of both dissolved concentration and precipitation of aggregates, has been characterized by ^{19}F-NMR quantification and DLS analysis. Precisely the measurements were taken immediately after the mixing (T_0), then after one day (T_1) and after six days (T_6) of room temperature storage. Afterwards, all the samples were mixed again with the same initial procedure (T_7), and characterized in order to check if it was possible to restore the initial dissolved concentration of salt.

3.3 Optimization of dissolution methods

All the samples listed in **Table 1** had an estimated starting salt concentration of 0.1 mM, which corresponds to 2.16 x 10^{18} ^{19}F atoms/mL. **Table 2** reports the quantification results obtained from ^{19}F-NMR spectra analysis taken at T_0, T_1, T_6 and T_7. NMR quantifications confirmed that the actual concentration of all samples was below the estimated one, meaning that $^{-}$AlR^{F} was not completely

soluble in water at 0.1 mM concentration and the fluctuating filaments and aggregates visible by eye belonged to undissolved $^{-}AlR^{F}$. Magnetic stirring alone was not able to give enough energy for complete salt dissolution (sample A), but increasing the temperature up to 50°C it was possible to almost double the previous concentration (sample B). Even if from this first result temperature seemed to be a key parameter to increase the solubility, when the boiling point of water was reached no further improvement of solubility was achieved, and the anion concentration according to ^{19}F-NMR was even lower (sample C). This might be due to the fact that at 100°C some $LiAlR^{F}$ might sublimate during the reflux (as suggested also by the DSC analysis of the salt). Better results were obtained using ultrasounds. In these cases, the temperature did not affect the salt solubility, that remained almost the same both in sample E and F, but increasing the energy by using tip sonication gave the highest concentration of dissolved fluorinated anion (sample G).

Table.2: Concentration of dissolved anion (mM) and number of fluorine atoms for each ml of sample, obtained with all the different dispersion methods after different times, as calculated from ^{19}F NMR quantification. For the NMR quantification, TFA was used as external standard as mentioned above.

Sample ID	**^{19}F atoms/mL at T_0**	**Concentration at T_0 (µM)**	**Concentration at T_1 (µM)**	**Concentration at T_6 (µM)**	**Concentration at T_7 (µM)**
A	$2.1x10^{17}$	10	10	9	10
B	$3.8x10^{17}$	20	20	18	20
C	$1.9x10^{17}$	8	8	7	8
D	$7.2x10^{17}$	38	36	32	36
E	$1.1x10^{18}$	50	48	48	49
F	$1.0x10^{18}$	48	46	46	48
G	$1.1x10^{18}$	53	50	49	49

As shown in **Fig. 17,** the different conditions used for dissolving the fluorinated salt did not affect the ^{19}F-NMR signal in terms of shape and chemical shift, giving always a sharp singlet peak with a chemical shift ranging from -75.20 to -75.28 ppm. Taking into account the stability over time, after six days the concentration of each sample slightly decreased (**Table 2**), however it was possible to restore the initial value simply by remixing the sample. This phenomenon is clearly visible in **Fig. 18,** where the intensity of the ^{19}F-NMR peak slightly decreased over time, without changing shape and chemical shift, and after remixing at T_7 the initial intensity was recovered. Although **Fig. 18** shows only the behaviour over time of sample G, the more concentrated one, the same trend was found also in all the other samples. This means that the quantity of $^{-}$AIR^{F} really dissolved in MQ water remained almost stable even after six days at room temperature.

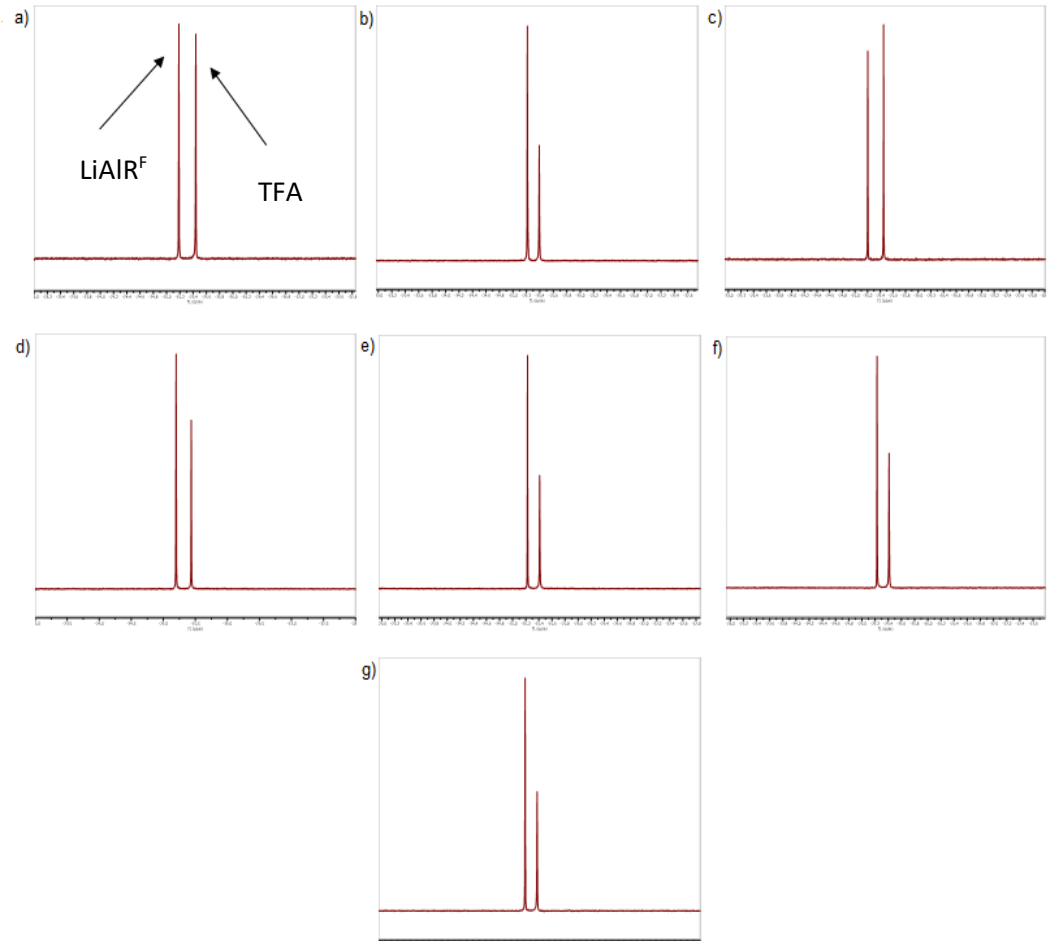

Figure 17. ^{19}F-NMR spectra of samples A-G (chemical shift range shown: from -74 to -77 ppm). In all spectra the peak on the left corresponds to the fluorinated anion, whereas the peak on the right is due to TFA external standard (-75.46 ppm): a) sample A, signal at -75.21 ppm, b) sample B at -75.21 ppm, c) sample C) at -75.20 ppm, d) sample D at -75.27 ppm, e) sample E) at -75.28 ppm, f) sample F at -75.27 ppm, g) sample G at -75.27 ppm.

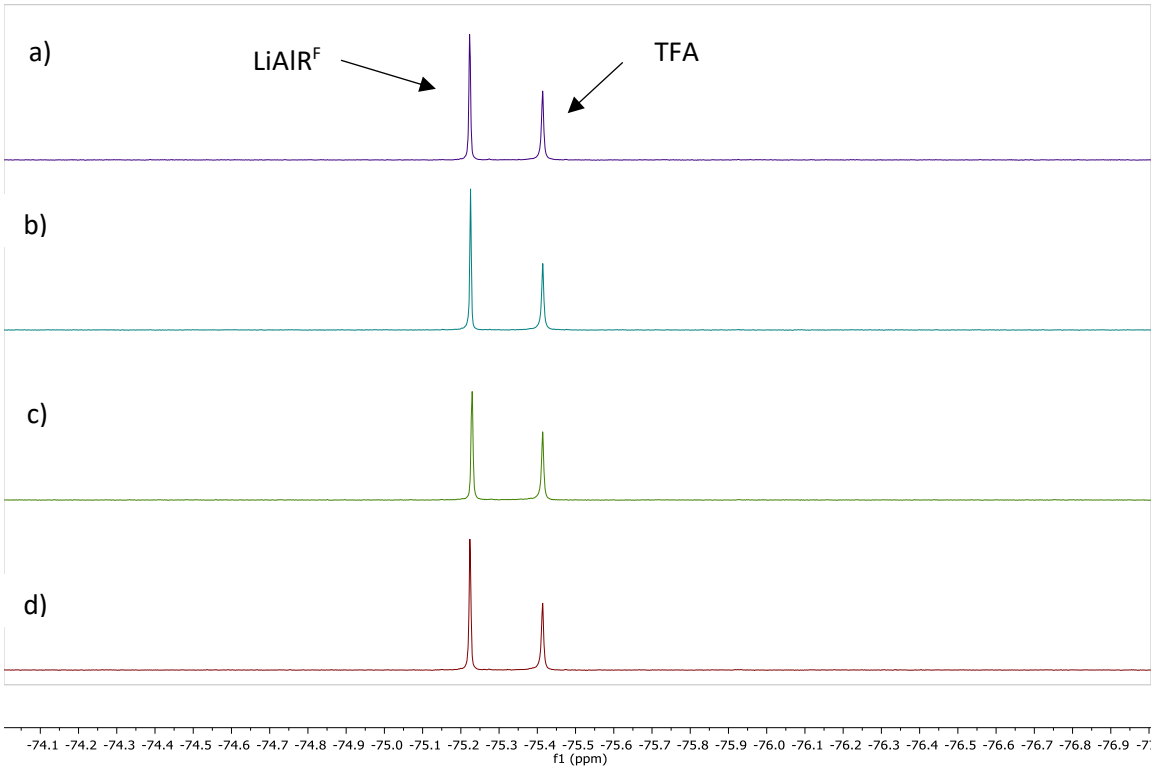

Figure. 18. NMR spectra of sample G at different times, stored at room temperature: a) immediately after preparation (T_0), b) after one day (T_1), c) after six days (T_6), d) after seven days the sample was remixed (T_7). All these spectra were acquired using the same TFA external standard as before.

Concerning DLS measurements, for the sake of clarity, the following discussion will focus only on the decay curves at 90°. Taking into account the dimension of scattering particles, the autocorrelation functions obtained from DLS analysis, **Fig. 19**, showed the presence of big aggregates with long decay times. As time went on, the autocorrelation functions exhibited an increase in the initial background noise and a decreases in scattering intensity, meaning that fluctuating particles were precipitating over time, as clearly visible in **Fig. 19, a-c** for the sample prepared by magnetic stirring. The previous observation was further confirmed by the fact that, after six days, some cororless precipiate was visible at the bottom of the vial. In the case of samples prepared by ultrasound treatment and tip sonication, **Fig.19, e-g**, no initial background noise was detected even after sample ageing, proving a higher particles stability in solution

with respect to the previous cases. Unfortunately, R_H values could not be estimated appropriately, because of the high polydispersity of the samples and also of the presence of aggregates with various shapes and sizes, as confirmed by TEM images, **Fig.20**.

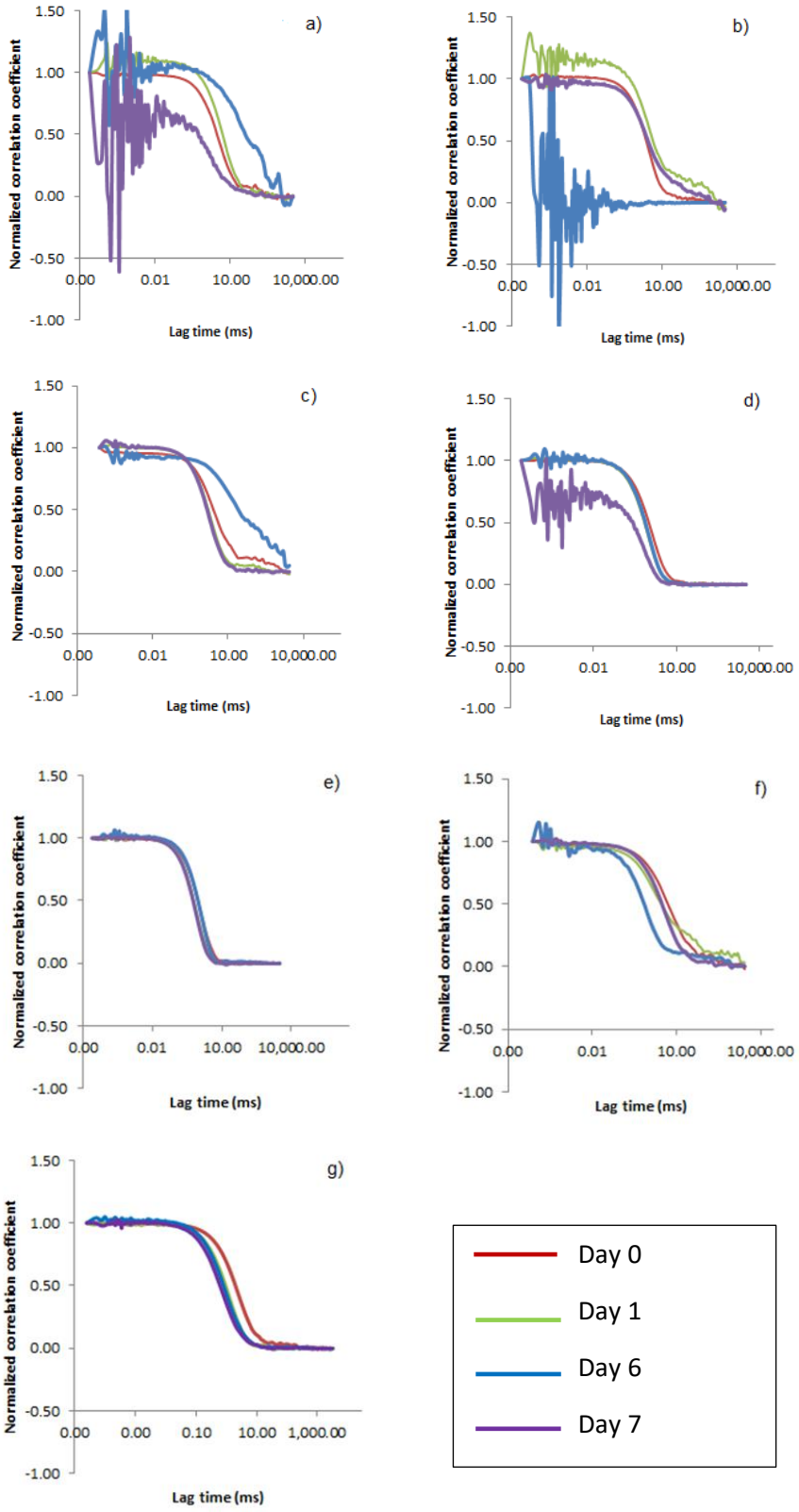

Figure 19: Autocorrelation functions at 90° measured at different ageing times: a) Sample A, b) Sample B, c) Sample C, d) Sample D, e) Sample E, f) Sample F, g) Sample G

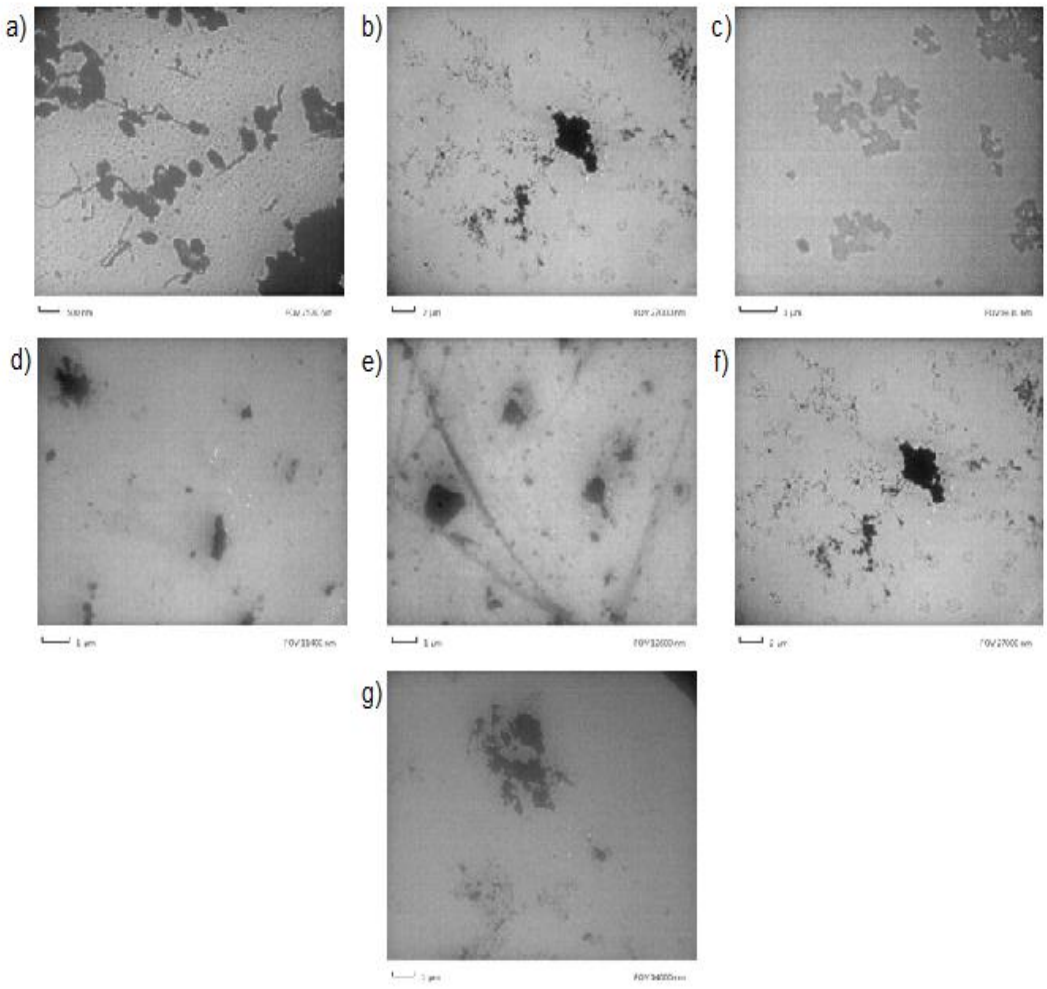

Figure 20. TEM images of: a) sample A and b) sample B. c) sample C, d) sample D, e) sample E, f) sample F, g) sample G.

3.4 Removal of aggregates

As previously mentioned in the first part of this chapter, $LiAlR^F$ is not highly soluble in water, but it tends to form dispersions with filaments and aggregates, partially visible even by eye. This impurities might affect ^{19}F-NMR quantifications, and consequently the determination of the real concentration of dissolved salt To remove these impurities, the samples with the highest number of fluorine atoms, sample E and G, were filtered and subsequently centrifuged, in order to try to

deposit these aggregates at the bottom of the Eppendorf tube. After each purification step, the supernatant was characterized by ^{19}F-NMR and DLS. The trend of DLS autocorrelation functions over time and the progressively formation of precipitate have shown that big aggregates tend to settle over time. The ^{19}F-NMR signal, on the other hand, was generated by fluorinated anions effectively dissolved in water and changed slightly with the aging of the sample. Starting from these observation, it was decided to try to purify the samples from the larger aggregates, which did not seem to contribute to the ^{19}F-NMR signal, in order to quantify more precisely how much fluorinated anion actually remained dissolved in water. In order to prove it, the dispersions of $LiAlR^F$ in water were treated by double filtration on a cellulose acetate (CA) 0.2 µm filter, followed by centrifugation at 1000 rpm for 30 minutes at 20°C. For this part of experimental work, only the most concentrated samples obtained before were chosen and tested: namely, sample E (ultrasound bath) and sample G (tip sonicator). Sample E and G were prepared following the same procedure described in chapter 3.3 and each of them was split into three aliquots of 3 mL volume. The first aliquot, called “initial”, consisted in the as-prepared sample. The second one was filtered twice on a 0.2 µm CA filter and will be termed as “filtered”. The last one, called “centrifuged”, was first filtered and then centrifuged. Comparing the characterization of the different aliquots, it was clearly visible that after filtration and centrifugation most of the bigger aggregates were removed from the samples. Each aliquot was characterized by ^{19}F NMR and DLS measurement, and the results are compared in **Fig. 21** and **Fig. 22**. The NMR spectra, **Fig. 21a** and **Fig. 22a**, confirmed that such aggregates did not affect the shape, the intensity and the chemical shift of the NMR signal that remained almost unchanged after each purification step. The removal of aggregates was experimentally confirmed also by the DLS autocorrelation functions, **Fig. 21b** and **Fig. 22b**, which showed an increase in the initial background noise after filtration and a flat autocorrelation function after centrifugation, corresponding to an almost complete removal of scattering aggregates. Therefore, these results demonstrated that bigger aggregates were not dissolved in water, and so they did not contribute to its ^{19}F-NMR signal and could be easily removed by filtration

and centrifugation. On the other hand, the stability over time of such NMR, which is due to the anion truly dissolved in water, proved that $^{-}AlR^{F}$ particles remain dissolved and did not interact with each other or aggregate with the passing of time.

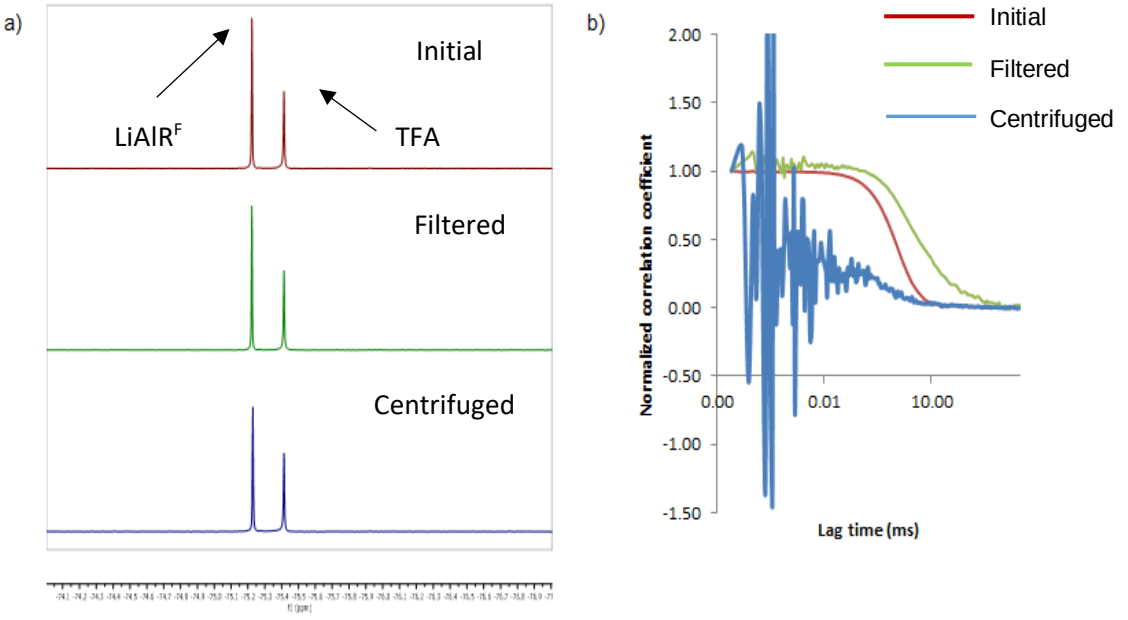

Figure 21. Characterization of sample E (ultrasound bath), as prepared and after purification: a) ^{19}F-NMR spectra of the 3 aliquots, showing only chemical shifts ranging from -74 ppm to -77 ppm; b) DLS autocorrelation functions at 90° measured 1 hour after each step.

Table.3 Chemical shift, number of fluorine atoms per mL of samples estimated from ^{19}F-NMR with TFA external standard, and concentration of dissolved anion calculated from the number of fluorine atoms.

Sample E	Chemical shift (ppm)	^{19}F atoms/ml (from NMR)	Concentration from NMR (µM)
Initial	-75.28	$1.1x10^{18}$	48
Filtered	-75.28	$1.0x10^{18}$	46
Centrifuged	-75.27	$1.1x10^{18}$	46

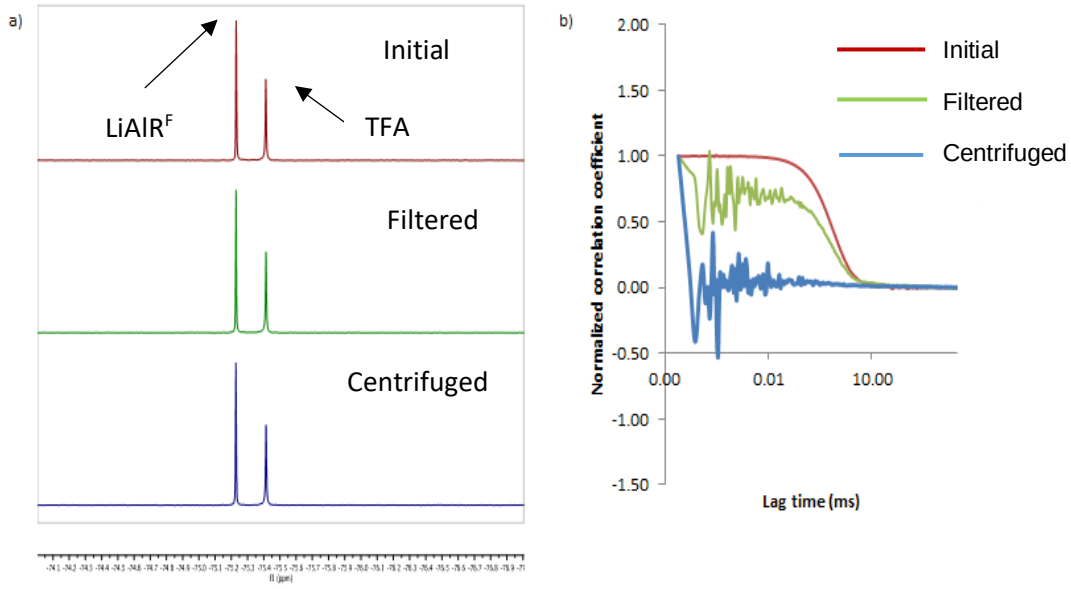

Figure 22: Characterization of sample G (tip sonicator), as prepared and after purification: a) ^{19}F NMR spectra of the 3 aliquots, showing only chemical shifts ranging from -74 ppm to -77 ppm; b) DLS autocorrelation functions at 90° measured 1 hour after each step.

Table 4 Chemical shift, number of fluorine atoms per mL of samples estimated from NMR with TFA external standard, and concentration of dissolved anion calculated from the number of fluorine atoms

Sample G	Chemical shift (ppm)	^{19}F atoms/ml (from NMR)	Concentration from NMR (µM)
Initial	-75.27	$1.1x10^{18}$	50
Filtered	-75.27	$1.1x10^{18}$	49
Centrifuged	-75.28	$1.1x10^{18}$	50

3.5 Stability in biological fluids

Once the maximum achievable concentration of fluorinated salt in water and its stability over time were assessed, the further step of this thesis' project consisted in checking the behaviour of $LiAlR^F$ in solvents whose characteristics are close to physiological media. As a first attempt, the salt was dissolved in a phosphate-

buffer saline (PBS) solution, and then in a solution of PBS containing 10% (v/v) of Fetal Bovine Serum (FBS) to verify the presence of interactions with proteins and biomolecules normally present in biological fluids. For this part of the experimental work, since the difference in concentration between sample E (ultrasound bath) and sample G (tip sonicator) is minimal, only the ultrasound bath method was used to dissolve the salt. Solutions were prepared by dissolving 1 mg of salt in 10 mL of PBS (sample H), or in 10 ml of PBS + 10% (v/v) FBS (sample I) respectively. All these samples were characterized by ^{19}F-NMR and DLS immediately after preparation and also after filtration followed by centrifugation, under the same conditions detailed in the previous paragraph. Further analyses were performed after five days of storage at room temperature. The shape of the ^{19}F-NMR peak in PBS did not change with respect to the ^{19}F-NMR peak in water, **Fig. 23a**, there was only a slight difference in the chemical shift **Fig. 23a** and **Table.3**. The quantification analysis from ^{19}F-NMR spectrum of sample H revealed a slightly increase in the concentration,56 μM with respect to 48 μM of sample E, **Table 5**. As reported in chapter 3.4 the filtration and centrifugation did not change the shape of the peak and the concentration, but after five days there was a slight decrease in the concentration, **Table 5**. The DLS analysis showed that the autocorrelation function of LiAlR^F dissolved in PBS, **Fig. 23b** (light blue curve), had a longer decay time with respect to the autocorrelation function belonging to simply PBS, **Fig. 23b** (yellow curve), this is due to the presence of big scattering aggregates formed during the dissolution of LiAlR^F. The double action of filtration and centrifugation removed some scattering aggregates, this is confirmed in **Fig. 23b** (red curve), where the corresponding autocorrelation function had a decay time close to neat PBS medium. After five days there was the formation of other scattering aggregates, as confirmed by the clear hump in the corresponding autocorrelation function, **Fig. 23b** (green curve), but this phenomenon did not alterate the concentration and the shape of the ^{19}F-NMR peak of the LiAlR^F because, as mentioned previously for water solution, even for PBS solution the ^{19}F-NMR signal was only affected by the $^-$AlR^F anions effectively dissolved. Some problems arised when LiAlR^F was dissolved in a solution of PBS with 10% (v/v) of FBS (sample I). The ^{19}F-NMR peak was still a

singlet, but it was no more narrow and intense as sample H, it became broader **Fig. 24a** with a decrease in the number of fluorine atoms dissolved, that corresponds to a lower concentration of $^{-}AlR^{F}$ anions in solution reported in **Table 5**. This might be due to the interaction of $^{-}AlR^{F}$ anions with serum proteins, that could interferer with ^{19}F-NMR detection. The filtration followed by centrifugation did not change the concentration, but differently from sample H, after five days there was a halving of the concentration, **Table 5**, with the ^{19}F-NMR peak becoming just barely visible, **Fig. 24a**; this means that in this media the sample was not stable over time. The DLS showed an increase in the decay time when $LiAlR^{F}$ was added to the solution, due to the presence of particle aggregates, **Fig. 24b** (light blue curve), with respect to a mixture of only PBS and FBS, **Fig. 24b** (yellow curve). Filtration and centrifugation removed the scattering aggregates and this corresponded to a decrease in the decay time, **Fig. 24b** (red curve); after five days, as in sample H, there was again an increase of the decay time, almost equal to the initial sample, with a hump in the autocorrelation function, **Fig .24b** (green line). This might be related to the formation of $^{-}AlR^{F}$ anions aggregagates over time whose size lead to an incease in the decay time, moreover this phenomenon could be connected to the decrease in the ^{19}F-NMR concentration.

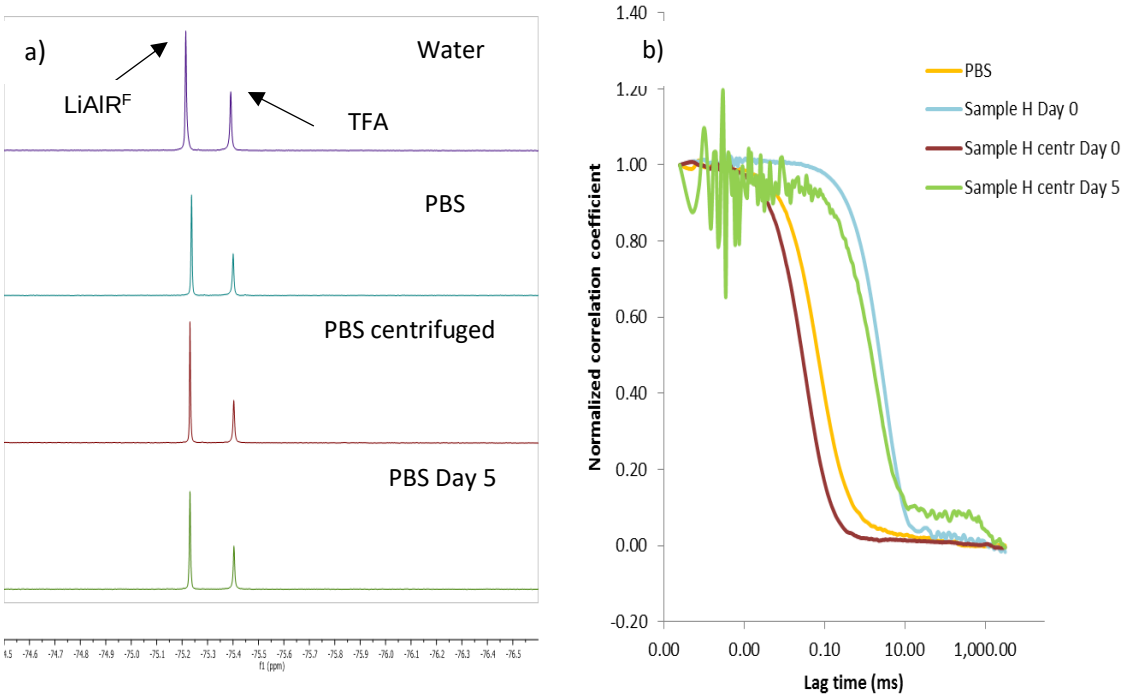

Figure 23. a) Comparison of ^{19}F-NMR spectra of LiAIR^F in PBS with the analogous sample in water (chemical shift range shown: from -74.5ppm to -76.5ppm) of sample E immediately after preparation in water (purple line) called ‘’water’’; sample H immediately after preparation in PBS (light blue line) ‘’PBS’’; sample H after filtration and centrifugation (red line), called ‘’PBS centrifuged’’; sample H after filtration and centrifugation, aged five days (green line) called ‘’ PBS Day 5’’. b) DLS autocorrelation functions of sample H taken at 90° at different conditions.

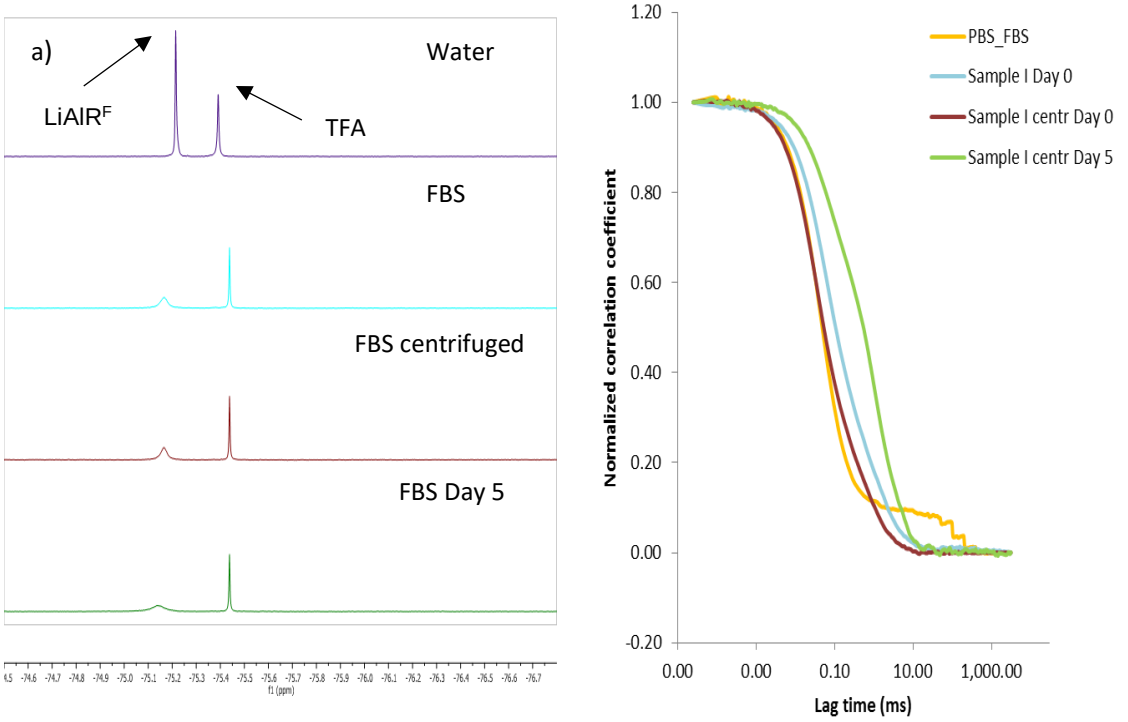

Figure 24. a) Comparison of ^{19}F-NMR spectra of LiAlR^{F} in PBS with 10% of FBS with the analogous sample in water (chemical shift range shown: from 74.5 ppm to -76.5 ppm) of sample E immediately after preparation in water (purple line) called ‘’water’’; sample I immediately after preparation in PBS/FBS solution (light blue line) called FBS; sample I after filtration and centrifugation (red line) called ‘’FBS centrifuged’’; sample I after filtration and centrifugation, aged five days (green line) called ‘’FBS Day 5’’. b) DLS autocorrelation functions of sample I taken at 90° at different conditions.

Table 5: Data collected from ^{19}F-NMR of -AlRF dissolved in water (sample E), in PBS (sample H), in a mixture of PBS/FBS (sample I). For the quantification it was used an external standard of TFA containing an absolute value of 3.43x10^{18} F/mLfluorine atoms. All the concentration are calculated starting from the ratio between the integral of $^{-}$AlR^{F} peak and the integral of TFA peak.

Sample	Chemical shift (ppm)	^{19}F atoms/ml (from NMR) at Day 0	Concentration from NMR (µM) at Day 0	Concentration from NMR (µM) After centrifugation at Day 0	Concentration from NMR (µM) After centrifugation at Day 5
E	-75.27	1.1x10^{18}	48	48	49
H	-75.30	1.2x10^{18}	56	54	52
I	-75.17	9.3x10^{17}	40	36	29

3.6 MRI preliminary test

Once established that $^{-}AlR^{F}$ anions dissolved in water gave a singlet, sharp peak in the ^{19}F-NMR and this peak was not perturbed by the removal of big aggregates by centrifugation, the last experiment performed on $LiAlR^{F}$ was a trial of phantom imaging acquisition by MRI. For this test, $LiAlR^{F}$ was dissolved in water by ultrasound bath, following the same procedure of sample E, then the solution was filtered and centrifuged as in the previous paragraphs. Before the MRI acquisition, 1 ml of supernatant was analysed measuring the relaxation time T_1 and T_2, which are respectively 2.18 and 1.53 seconds. These relaxation times were long compared to other contrast media, and this bode well for imaging. Then other 2 mL of supernatant were withdrawn and sent to San Raffaele Hospital, where Dr. Linda Chaabane kindly performed the MRI phantom acquisition test. The experiment was performed with a 7-T imager (Biospec, Bruker Biospin, Germany) using a dual transmit-receive $^{19}F/^{1}H$ volume coil. A two-dimensional turbo spin-echo sequence was used with a field of view of 10 x 10 mm (53 minutes of acquisition, 100 signal averages) at low spatial resolution (pixel 1.56 x 1.25 mm), **Fig. 25**. It was possible to observe the presence of some scattered blur spot, which is a promising result for what concern the applicability of $LiAlR^{F}$ as a possible ^{19}F-MRI probe because, even if it was weakly visible, it was detected by the instrument. Regrettably, it was not possible to obtain a single clear spot, due to low quality and low resolution image; this could be a consequence of the fact that the concentration of sample E is $1.15x10^{18}$ F/ml and this value is closer to the detection limit of the instrument.

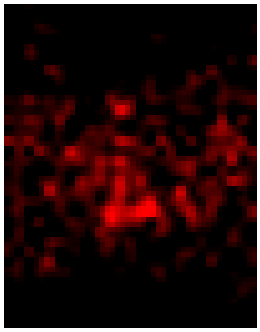

Figure 25: MRI phantom of sample E

Chapter 4: Conclusion and future perspectives

This thesis' project was aimed to perform a preliminary study to assess if the highly fluorinated anion of a $LiAlR^F$ salt could be used as ^{19}F-MRI probe, starting from its solubility in water. From the first dissolution experiments it was ascertained that $LiAlR^F$ is slightly soluble in water, with the formation of precipitate and fluctuating visible aggregates due to the interaction between undissolved $^-AlR^F$ anions. Nevertheless, ^{19}F-NMR spectra showed a singlet, sharp peak generated by the anions dissolved in water. In the following step, different dissolution methods, using magnetic stirring, ultrasound bath and tip sonicator under variable conditions of time and temperature, were carried out to increase the solubility of $LiAlR^F$ in water, starting from an estimated concentration of 0.1 mM. Among all the methods tested, the use of the ultrasound bath (sample E) at room temperature and the tip sonicator treatment (sample G) have given the higher concentration of dissolved fluorinated anions, respectively 48 and 50 μM. Moreover, these solutions exhibited stability over time, without changing such initial concentrations, as proved by ^{19}F-NMR. DLS autocorrelation functions measured on the same samples showed the presence of big scattering particles. Unfortunately, it was not possible to estimate their R_H due to their high polydispersity and to the presence of aggregates with irregular shapes, as confirmed by TEM images. The two more concentrated samples were then purified, removing fluctuating aggregates by a double filtration followed by centrifugation, and they were characterized by ^{19}F-NMR and DLS after each removal process. DLS analysis confirmed the removal of the big scattering aggregates, because the autocorrelation functions exhibited an increase in the background noise after double filtration and they became almost flat after centrifugation. Surprisingly, ^{19}F-NMR spectra did not show any change in shape and concentration even over time in both samples after purification, meaning that the ^{19}F-NMR signal came only from $^-AlR^F$ anions effectively dissolved in water and such anions were not removed by either filtration or centrifugation. Once evaluated the maximum concentration in water and confirmed that the removal

of aggregates did not influence ^{19}F-NMR signal, dissolution tests have been carried out in solvents that are closer to physiological conditions in the human body, trying first with PBS and successively with a mixture of PBS and 10% (v/v) of FBS. The behaviour of LiAlR^{F} in PBS is similar to that in water, showing a singlet, sharp peak in ^{19}F-NMR spectra, but with a slight increase in the anion concentration (56 μM in sample H); this trend was kept even over time. By adding a small quantity of FBS, on the other hand, the concentration of fluorinated anion in solution decreased and the NMR peak of $^{-}$AlR^{F} became broader, maybe due to some kind of interactions with serum proteins, until the signal almost disappeared after five days. To further verify the possible application of LiAlR^{F} as a ^{19}F MRI probe, a preliminary trial of phantom imaging by ^{19}F-MRI was performed. The image did not display a clear and focused red spot, but a poor-quality image with almost single pixels visible, due to the fact that the phantom fluorine concentration was too close to the limit of detection of the instrument. Nevertheless, this was a desirable and promising result that confirmed the possibility of using LiAlR^{F} as a ^{19}F MRI probe thanks to its singlet, sharp ^{19}F-NMR peak in water. Obviously, if this highly fluorinated anion is directly dissolved in water, its concentration is too close to the detection limit of ^{19}F-MRI to be effectively applicable. Therefore, its use for imaging purposes require a further optimization of the dispersion protocol in water, in order to go beyond the detection limit of ^{19}F-MRI. A possible future strategy could envisage increasing the duration of tip sonication, or trying to encapsulate the anion into some biocompatible and water-soluble carrier, such as PLGA, [43] or its coating by some naturally occurring amphiphilic surfactant proteins [44]. This encapsulation strategy could also be useful to avoid undesired and destabilizing interactions with physiological liquids, that seem to induce alteration and even loss of the ^{19}F-NMR signal.

Bibliography

[1] Tarik F. Massoud et al. ‘Molecular imaging in living subjects: seeing fundamental biological processes in a new light’. Genes & development, 2003. Volume 17: 545-580.

[2] Michelle L. James et al. ‘A Molecular Imaging Primer: Modalities, Imaging Agents, and Applications’. Physiological Reviews 2012. Volume 92: 897-965.

[3] Shahriar S Yaghoubi et al. ‘Noninvasive detection of therapeutic cytolytic T cells with 18F–FHBG PET in a patient with glioma’. Nature Clinical Practice Oncology, 2009. Volume 6: 53–58.

[4] Siti M.Janib et al. ‘Imaging and drug delivery using theranostic nanoparticles’. In: Advanced Drug Delivery Reviews, 2010, Volume 62: 1052-1063.

[5] J.R. Alger et al. ‘Magnetic Resonance Spectroscopy’. In: Encyclopedia of Neuroscience, 2009, 601-607.

[6] Galal Omami et al. ‘Basic principles and applications of 18F-FDG-PET/CT in oral and maxillofacial imaging: A pictorial essay’. Imaging Science in Dentistry, 2014 Volume 44: 325-332.

[7] Wai-Hoi Gary at al. ‘Principles of Single Photon Emission Computed Tomography and Positron Emission Tomography’. In: Targeted Molecular Imaging in Oncology, 2001. Springer,19-29.

[8] P. C. Lauterbur et al. ‘Image Formation by Induced Local Interactions: Examples Employing Nuclear Magnetic Resonance’. Nature, 1973. Volume 242, 190–191.

[9] Vijay P.B. Grover et al. ‘Magnetic Resonance Imaging: Principles and Techniques: Lessons for Clinicians’. Journal of Clinical and Experimental Hepatology 2015. Volume 5: 246–255.

[10] Markus Weiger et al. ‘Short-T2 MRI: Principles and recent advances’. Progress in Nuclear Magnetic Resonance Spectroscopy, 2019. Volumes 114–115: 237-270.

[11] Zhao Ling-Yuna et al.’ Magnetic-mediated hyperthermia for cancer treatment : Research progress and clinical trials’. Chinese Physical Society, 2013. Volume. 22(10).

[12] R. A. Pooley et al.’Fundamental Physics of MR Imaging’, RadioGraphics, 2005. Volume 25: 1087-1099.

[13] David P.Cormode et al. ‘Modified natural nanoparticles as contrast agents for medical imaging’. In Advanced Drug Delivery Reviews, 2010. Volume 62: 329-338.

[14] Mangala Srinivas et al. ’19F MRI for quantitative in vivo cell tracking’. Trends in biotechnology, 2010. Volume 28: 363-37.

[15] Ilaria Tirotta et al. ‘19F Magnetic Resonance Imaging (MRI): From Design of Materials to Clinical Applications’. Chemical Reviews. 2015. Volume 28; 115(2):1106-29.

[16] Tran, T.D. et al. ‘Clinical applications of perfluorocarbon nanoparticles for molecular imaging and targeted therapeutics. International Journal of Nanomedicine. 2007. Volume 2: 515–526.

[17] Marie Pierre Krafft et al. ‘Perfluorocarbons: Life sciences and biomedical uses’. Polymer Science, 2007. Volume 45: 1185-1198.

[18] Xia et al. ‘Tumour oxygen dynamics measured simultaneously by near-infrared spectroscopy and 19F magnetic resonance imaging in rats’ .In: Physics in Medicine & Biology, IOP Publishing Ltd, 2006. Volume 51: 1070-1090.

[19] Wolfson Marla et al. ‘Pulmonary applications of perfluorochemical liquids: ventilation and beyond’. In: Paediatric respiratory reviews Paediatric, 2005. Volume 6: 117-127.

[20] Schwarz et al.'19F-MRI of perfluorononane as a novel contrast modality for gastrointestinal imaging'. Magnetic Resonance in Medicine 1999, Volume 41: 80-86.

[21] Kaneda Megan et al. 'Perfluorocarbon nanoemulsions for quantitative molecular imaging and targeted therapeutics'. In: Annals of biomedical engineering, Springer, 2009. Volume 37: 1922–1933.

[22] Fatihah Suja et al. 'Contamination, bioaccumulation and toxic effects of perfluorinated chemicals (PFCs) in the water environment. In: Water Science & Technology, IWA Publishing 2009. Volume 60: 1533–1544.

[23] Z. Wang et al. 'Fluorinated alternatives to long- chain perfluoroalkyl carboxylic acids (PFCAs), perfluoroalkane sulfonic acids (PFSAs) and their potential precursors'. Environment International 2013. Volume 60: 242−248.

[24] Ahrens et al.'In vivo imaging platform for tracking immunotherapeutic cells'. In: Nature Biotechnology, 2005. Volume 23: 983–987.

[25]. Ilaria Tirotta et al. 'A Superfluorinated Molecular Probe for Highly Sensitive in Vivo19F-MRI. Journal of the American Chemical Society 2014. Volume 136: 8524–8527.

[26] Olga Koshkina et al. 'Nanoparticles for ''two color" 19F magnetic resonance imaging: Towards combined imaging of biodistribution and degradation'. In: Journal of Colloid and Interface Science, Elsevier. Volume 565: 278–287.

[27] Cristina Chirizzi et al. 'Multispectral MRI with Dual Fluorinated Probes to Track Mononuclear Cell Activity in Mice'. Radiology 2019 Volume 291:351–357.

[28] Ian M. Riddlestone et al. 'Taming the Cationic Beast: Novel Developments in the Synthesis and Application of Weakly Coordinating Anions'. A Journal Of The German Chemical Society. 2018. Volume 57, 13982 – 14024

[29] Ingo Krossing et al. 'Chemistry with weakly-coordinating fluorinated alkoxyaluminate anions: Gas phase cations in condensed phases?'. In: Coordination Chemistry Reviews , Elsevier, 2006. Volume 250: 2721–2744.

[30] I Krossing et al.'Weakly Coordinating Anions: Fluorinated Alkoxyaluminates. In: Comprehensive Inorganic Chemistry II, Elsevier 2013 Volume 1: 681-704.

[31] Ines Raabe Dr. et al. 'Tetraalkylammonium Salts of Weakly Coordinating Aluminates: Ionic Liquids, Materials for Electrochemical Applications and Useful Compounds for Anion Investigation'. Chemistry an European Journal 2009. Volume15: 1966-1976.

[32] Maria Kaliner et al. 'Tunable aryl alkyl ionic liquids with weakly coordinating bulky borate anion'.In: Tetrahedron Letters, Elsevier 2016. Volume 57: 3453-3456.

[33]. Bohdan Andreiuk et al. 'An aluminium-based fluorinated counterion for enhanced encapsulation and emission of dyes in biodegradable polymer nanoparticles'. The Royal Society of Chemistry, 2017. Volume 1: 2309-2316.

[34] Jörg Stetefeld et al. 'Dynamic light scattering: a practical guide and applications in biomedical sciences . Biophysical Reviews , 2106. Volume 8: 409–427.

[35] Anton Paar.The principles of dynamic light scattering. https://wiki.anton-paar.com/it-it/i-principi-della-diffrazione-dinamica-della-luce/

[36] William F. Reynolds et al. 'Nuclear Magnetic Resonance in the Structural Elucidation of Natural Products'. In: Progress in the Chemistry of Organic Natural Products, Springer, 2015. Volume 100: 223-309.

[37].Nuclear Magnetic Resonance Spectroscopy. https://www2.chemistry.msu.edu/faculty/reusch/virttxtjml/spectrpy/nmr/nmr1.htm

[38] Overview of Electron Microscopyn. https://authors.library.caltech.edu/5456/1/hrst.mit.edu/hrs/materials/public/ElectronMicroscope/EM_HistOverview.htm

[39] Transmission Electron Microscopy Study of Domains in Ferroelectrics, Doctoral Thesis by Kristina Holsgrove, School of Mathematics and Physics, Queen's University Belfast, 2017

[40] N. D. Browning et al.' Atomic-resolution chemical analysis using a scanning transmission electron microscope. Nature, 1993. Volume 366: 143–146.

[41] Da Shi et al. 'Microbubbles decorated with dendronized magnetic nanoparticles for biomedical imaging: effective stabilization via fluorous interactions'. Beilstein J. Nanotechnol. 2019. Volume 10: 2103–2115.

[42] Csongor Szíjjártó et al. 'Effects of Perfluorocarbon Gases on the Size and Stability Characteristics of Phospholipid-Coated Microbubbles: Osmotic Effect versus Interfacial Film Stabilization'. In: Langmuir, American Chemical Society, 2012. Volume 28: 1182–1189

[43] Mirkka Sarparanta et al. 'Intravenous Delivery of Hydrophobin-Functionalized Porous Silicon Nanoparticles: Stability, Plasma Protein Adsorption and Biodistribution'. In: Molecular Farmaceutics, American Chemical Society, 2012. Volume 9: 654–663.

[44] M.S.Grunér et al. 'An environmental route of exposure affects the formation of nanoparticle coronas in blood plasma'. Journal of Proteomics, 2016. Volume 137: 52-58